Chipiron
High quality 1 mT MRI

Zineb Belkacemi, Yacine Belkhodja, Romain Couvreur, Bastien Dassonneville, Guillaume Daval-Frerot, Marco Fiorito, Eva Grimaldi, Alexandre Jaoui, Ijee Mohanty, Isabelle Saniour, Sara Varotto and Dimitri Labat*
Chipiron - 2-8 rue Gaston Rebuffat, 75019 Paris
(Dated: March 28, 2024)

This paper gives a bit of context about what we are currently building at Chipiron. It is by no means a formal introduction to the physics of SQUIDs or MRI. Rather, it is a sort of *teaser* to our global project: make MRI as easy as routine blood sampling so it finally becomes accessible to everyone, everywhere, with no compromise on image quality. Because we give quantitative details about our technological strategy, the reader should have some basic knowledge of undergrad-level math and physics to make the most out of the content, though a lot of parts should be accessible to all (maybe with a little effort).

This paper was written with three kinds of readers in mind: enthusiast **VCs and angel investors** who want to understand what's under the hood; **engineers and medical device professionals**, who would be interested in joining our mission; and **physicians**, who might reasonably be skeptical hearing about an MRI machine the size of a little closet.

We will start by giving non-physicists a brief explanation of what is an MRI experiment, and some flavour of the quantum physics governing the operation of a SQUID. Then, we will lay out the global landscape of what's already been done in 20 years of research in ultra-low field MRI, in particular SQUID-detected MRI. After that, we will lay out our technological strategy to improve the image quality from the state-of the art, to finally make clinical ultra-low field MRI a reality.

Please reach out to shoot your comments and questions! dimitri@chipiron.co

EXECUTIVE SUMMARY - PITCH

Magnetic resonance imaging (MRI) is the most powerful medical imaging technique, yet it remains dramatically inaccessible to 80% of the world's population.

There are several factors preventing a global adoption of MRI:

- It is extremely expensive: count about $2M in CapEx and OpEx over the whole lifespan of the machine.
- More importantly, it is very cumbersome to operate MRI machines. They lie in tech-heavy magnetically-shielded rooms at the core of hospitals, require a very stable high-consumption electricity network, weigh more than 5 tons which requires a crane and special floor reinforcement to install.
- A sizeable fraction of the population has no access to MRI: obese or claustrophobic patients, patients equipped with pacemakers or other implants, or unconscious subjects, all of which are very common in day-to-day operation.

At the root of these problems lies the huge magnetic field needed to conduct MRI experiments. This field is produced by enormous expensive superconducting magnets. In over 40 years of existence, the paradigm in the MRI industry has always been to go for higher and higher fields. In fact, high fields allow gathering great quantities of signal, meaning better images in shorter acquisition times. However, one of the key parameters governing the quality of the images is not precisely the quantity of signal, but rather the signal-to-noise ratio (SNR). The only way to solve the problem of MRI accessibility is to work at low fields, with light magnets. It is still possible to keep a good SNR at low fields if the noise is reduced by the same amount. At Chipiron, we build a transportable MRI machine the size of a little closet, working at fields one thousand time lower, powered by a patented ultra-sensitive detection device based on SQUID (superconducting quantum interference device) technology. The unique contrasts at ultra-low fields will open new imaging procedures and improved diagnosis capabilities. This machine will make MRI as accessible as routine blood sampling.

WHAT IS A SQUID? HOW CAN WE USE IT TO IMPROVE MRI?

The MRI experiment

Magnetic resonance: principles

The goal of an MRI (magnetic resonance imaging) experiment is to image the inside of the human body. This image takes the form of a 2D pile of 3D slices. The technique is based on the phenomenon of *nuclear magnetic resonance* (NMR) of the protons inside the body. These protons (hydrogen nuclei) are present in every organ and part of the body in different proportions, mostly as part of water, fat, or tissue molecules.

The part of the body we want to image (i.e. the *sample*) is placed in a very homogeneous static magnetic field B_0 called the *polarization field*. In most commercial devices, this magnetic field has a high intensity of either 1.5 or 3.0 Tesla. This field is produced by a big coil made of superconducting material, this is the big "tunnel" in which you enter when doing an MRI scan. When protons of the body are placed in a magnetic field B_0, they precess about the magnetic field with a frequency ω_0 given by $\omega_0 = \gamma B_0$, where $\gamma \simeq 42$ MHz.T^{-1} is called the gyromagnetic ratio of the proton. More precisely, when we say protons 'align", is because they carry a *spin*, which is a quantum property that has a lot of similarities with classical magnetic moment. One can think of protons as tiny magnets. The goal of the MRI experiment is to excite the protons thanks to a radiofrequency signal of the same frequency $\omega = \omega_0$ as the precession of the protons. This excitation will knock the protons out of their precession movement, after a while they will slowly decay back to their original precession state while emitting a signal that we detect with an antenna. The measure of this signal, more precisely its decay time, is a way to gather information about the composition of the inside of the body, and ultimately to reconstruct an MRI image.

So let's sum up the global principle of the MRI experiment:

1. The part of the body to image is placed in a static homogeneous magnetic field B_0. In most machines this field is of intensity of order 1 T. At Chipiron, we plan to use fields one thousand times lower.

2. When placed in this field the protons precess with a frequency $\omega_0 = \gamma B_0$.

3. Thanks to an excitation antenna, we send a pulse of intensity B_1 and frequency $\omega = \omega_0$ tuned to the precession of the protons.

4. The protons are sent to a higher energy state and decay back to their original state while sending off a signal of intensity B_2 and frequency ω_0. Most importantly, their signal decay with typical times T_1 and T_2 which are characteristics of tissues of the body.

Field intensity

The usual paradigm in MRI is to go for higher and higher fields, for two main reasons. The first one is that a higher field means a higher polarization of the sample. This polarization represents the fraction of protons that participate in the MRI signal. In fact, only a very tiny fraction of the protons get affected by the polarization field B_0 [1]. The higher the field, the higher the polarization and the most signal gets emitted by the protons. This leads to better images and a reduced time of acquisition for the experiment.

The second reason why high fields are useful is that the sensitivity of the antenna is proportional to the frequency at which we work, ω. Taking into account the thermal noise inside the antenna, that goes as $\omega^{1/4}$, the detection threshold scales as $\omega^{-3/4}$ [2]. This detection threshold represents the smallest signal per unit bandwidth that we are able to measure out of the background noise. As we have seen previously, the frequency scales as $\omega = \gamma B_0$. Working at high frequency, hence high field, allows us to have a smaller detection threshold, which guarantees a higher signal-to-noise ratio and a smaller time of acquisition. Usually, in MRI experiments, the signal you measure is very low, and you have to repeat the acquisition, or sequence, N times to average the background noise. In high field experiments where the signal is larger, you can just do $N = 1$ or just a few repetitions, while in low field experiments N can easily be in the hundreds.

However, working at high fields comes with a lot of drawbacks, both technical and non-technical. From an image quality perspective, the use of high field is often associated with high resolution and good image quality. While this is certainly true, high fields also provoke ionic noise inside the sample and perturbations due to differences in magnetic susceptibilities between tissues [3]. This creates artifacts that degrade image quality. Also, contrasts tend to be lower at higher fields, most notably T_1 contrast, because T_1 values of different tissues converge to similar values (see next part). For these reasons, working at ultra-low fields can unlock new imaging capabilities. From a non-technical point of view, high-field MRIs are expensive, complex to operate, and require heavy infrastructure. Even in rich, well-equipped countries, access to an MRI scan is limited, and a large portion of the population is deprived of MRI: persons suffering from claustrophobia, obesity, carrying pacemakers, or soldiers with bullet wounds, just to mention a few.

A typical clinical MRI machine works at either $B_0 =$ 1.5 or 3 T. [4] We at Chipiron take the absolute opposite approach: instead of going for high-fields, we will work three orders of magnitude below clinical standards, around $B_0 = 1$ mT, using ultra-sensitive detection to counterbalance the loss of signal. In fact, the important parameter in the experiment is not the intensity of the signal itself but rather the signal-to-noise ratio (SNR). Lowering both the field AND the noise, and using a very sensitive detection system, we are able to keep the same SNR working at ultra-low-field, thus preserving an image quality on par with today's clinical standards at a fraction of the cost and opening a whole new range of applications.

How do you construct an image? Gradients and sequences

So far, we've only explained how protons emit magnetic resonance signal across the whole body. To construct an image, we need to be able to tell where does the signal that gets detected by the MRI antenna comes from. This is where gradient coils come into play. On top of the permanent homogeneous B_0 field, we will add a small supplementary field $\delta B(x, y, z)$ that varies linearly along all three space directions. Typically, in a commercial 1.5 T device you have δB of order 100 $\mathrm{mT.m^{-1}}$. The gradient field is produced by three *gradient coils* installed in the MRI machine near the polarization field coil.

Let's consider the case of 2D imaging where the 3D image is produced by a pile of successive 2D slices. The gradient coils produce a small field $\delta B(x, y) = G_x x + G_y y$ on top of the homogeneous B_0 field. The field felt by a proton at point (x, y) in the slice will then be $B_0 + \delta B(x, y)$. Following earlier discussions, this proton will rotate about the field with a frequency $\omega(x, y) = \gamma\left(B_0 + \delta B(x, y)\right)$ that depends on the position (x, y) of the proton.

To be able to make an image, your goal is to tell from which *voxel* (or 3D pixel) the signal comes from, and it is precisely what the gradients are made for. Typically, during the sequence, you will first apply a *phase-encoding* gradient G_y for a short duration. After this duration, protons with different y positions in the image will be out of phase because they spun at different frequencies during the phase-encoding step. Then, we apply the *frequency-encoding* gradient G_x and acquire the NMR signal. This procedure is repeated N_p times with varying G_y intensities, where N_p is the number of phase-encoding steps. In the end, the phase of the NMR signal carries information about the y position of the voxel, while the frequency information is contained in the frequency of the signal. A 3D image is constructed by repeating this for the N_s slices, with the help of the G_z gradient and a selective RF excitation pulse which is tuned to a precise z slice.

The duration, intensity, and order in which you apply the different gradients and excitation fields is called an *MRI sequence*. Different sequences allow us to see images contrasted in different ways. In fact, certain sequences will highlight tissues with long T_1, we call it a T_1-weighted sequence. While contrast in a CT scan image results from only one parameter, namely the rate of absorption of X rays by tissues, MRI images can be contrasted by a large number of parameters, which relative weights depend on the sequence used: T_1, T_2, proton density, magnetic susceptibility, water diffusion tensor, for instance. More recently, there has been a surge in interest for *quantitative* sequences such as magnetic resonance fingerprinting that produce maps of local parameters, such as T_1 and T_2, instead of *qualitative* images that are weighted by a wide range of parameters. The versatility of MRI is one of its greatest assets, and is the main reason why it holds such a special spot among all medical imaging techniques.

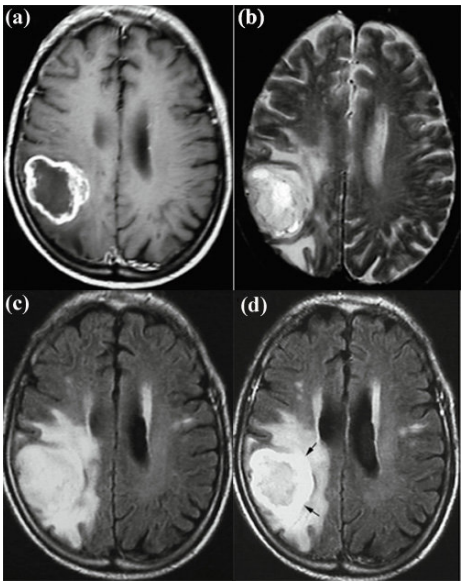

FIG. 1. The same brain seen by different MRI sequences. (a) T1-weighted. (b) T2-weighted. (c) FLAIR. (d) FLAIR with contrast enhancement. *Liu et al , Tsinghua Science and Technology* ***19****(6):578-595 (2014)*

Classical or quantum antennas

The core of our innovation is an ultrasensitive magnetic detection system. In every MRI experiment you need a way to detect the signal emitted by the sample. This signal is a RF decaying pulse, for instance, in a 1.5 T experiment its central frequency is about 60 MHz. At these frequencies, it is convenient to use an inductive antenna, which is simply a closed loop of surface S made of copper wire. When an electromagnetic signal goes through the loop, by Faraday's law,

$$Ri = -\frac{d\Phi}{dt}, \tag{1}$$

where i is the intensity of the current generated inside the loop, R is the loop's ohmic resistance, and $\Phi = B_2 S$ is the flux of the magnetic part B_2 of the signal going through the loop [5]. If we consider a signal of frequency ω_0 tuned to the working frequency $\omega_0 = \gamma B_0$, the relation between the current inside the antenna and the polarization field B_0 is simply

$$i = \frac{1}{R}\gamma B_0 B_2 S. \tag{2}$$

Having a sensitive antenna means having a high current i inside the antenna for a given field B_2 to measure. From

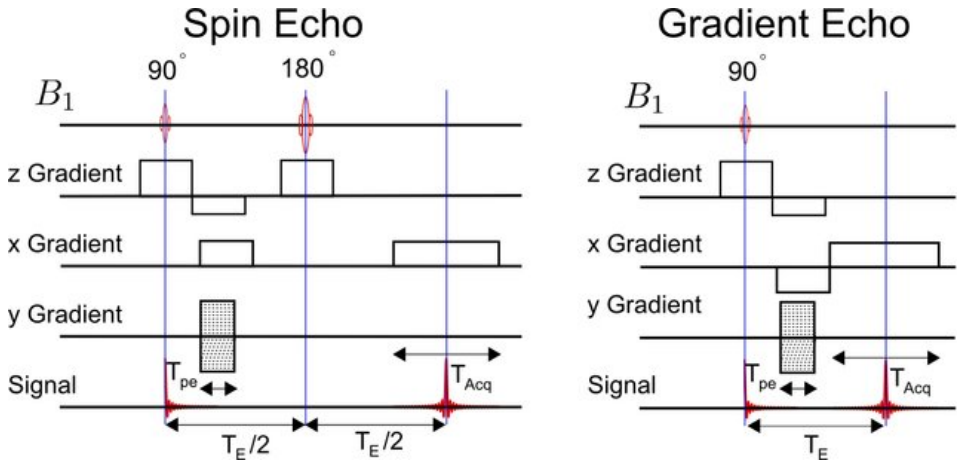

FIG. 2. Field intensity with respect to time for spin-echo and gradient-echo type of sequences, which are the two main families of MRI sequences. B_1 is the excitation field. While the spin echo sequence uses an additional excitation pulse to rephase the spins (hence the name "spin echo"), in the case of the gradient echo sequence, the echo is produced by the successive dephasing and rephasing of the frequency-encoding X gradient. Spin echo sequences are one of the earliest developments of MRI. Gradient echo sequences tend to be faster but are more sensitive to image artifacts. PhD thesis of Karl Edler.

the previous equation one can see that inductive antennas are going to be much more efficient at high magnetic fields. If we want to work at low fields, let's say lowering it from 1.5 T to 1 mT, the antenna is going to be 1500 times less powerful. A potential way to tackle this problem would be to decrease the resistance R, which can be done by cooling down the antenna, for instance by immersing it into liquid Nitrogen. But there is no way to win a factor 1500 on sensitivity with such a simple process.

This is where SQUIDs come into play. Unlike inductive antennas, they have a flat frequency response over a wide band, meaning that their sensitivity does not depend on frequency. This comes from the fact that SQUIDs are *pure transducers*, they are directly sensitive to the magnetic field itself while a classical antenna is sensitive to its temporal derivative. A direct consequence of this is that the lower the field you use, the better the SQUID is going to be compared to the classical antenna, making them very good candidates for magnetic detection at ultralow fields.

SQUIDs also have two other advantages: their exquisite sensitivity, and their very low intrinsic noise of a few 0.1 pA.Hz$^{-1/2}$ [6]. These two characteristics allow to have a detection threshold, which is the smallest signal that you can measure per unit bandwidth, below 1 fT.Hz$^{-1/2}$ at very low fields. Our goal is to go even beyond, approaching 0.1 fT/$\sqrt{\text{Hz}}$ which would, in theory (see fig. 3), give equivalent signal-to-noise as 0.2 T MRI with all the additional advantages of the ultra-low field.

More precisely, we can get a general flavour on the relative performance of SQUIDs and classical inductive antennas as follows. For a given background noise, the detection threshold roughly scales as the ratio between the detected signal and the detector noise. For an inductive antenna, the signal in the antenna is given by Faraday's law $e = -\frac{d\Phi}{dt}$ and scales as ω_0^2 (factor of ω_0 for the field and another ω_0 for the time derivative). On the other hand, Johnson noise, which is the main source of noise in the detector, goes as $\omega_0^{1/4}$ (Johnson noise is in $\sqrt{R}$, R being DC resistance, which is itself in $\sqrt{\omega}$ because of skin effect in conductors). It follows that the detection threshold of an inductive antenna goes as $\omega^{-3/4}$.

In the case of SQUIDs, the detection threshold goes simply as ω_0. In fact, the detector is directly sensitive to the field which gives a factor of ω_0, while the intrinsic noise remains constant over a wide range of frequencies. Comparing the two cases, we can see that there is a crossover regarding the relative detection thresholds of SQUIDs and inductive antennas. As is well explained in the figure 3, above a typical frequency of $\sim$ 20 mT inductive antennas start to have better detection threshold. A more in-depth discussion of the relative performances of SQUID and inductive detection systems for MRI can be found in a paper of the Berkeley team [7].

There is a large variety of magnetic detection systems that could be good candidates for MRI detection, but SQUIDs are the more technologically mature of them. Even 60 years after their discovery, SQUIDs continue to hold a special place, mainly because of their extreme sensitivity combined with a very broad bandwidth (up to a few tens of MHz [8]). Below we list a few other options.

- Optically pumped magnetometers (OPMs) based on alkali vapour cells have raised a lot f excitement in the past years as they can reach extremely high sensitivities up to just above 0.1 fT.Hz^{-1} [9] and have been used to perform pre-polarized MRI at 4 mT [10]. However, they suffer from notable draw-

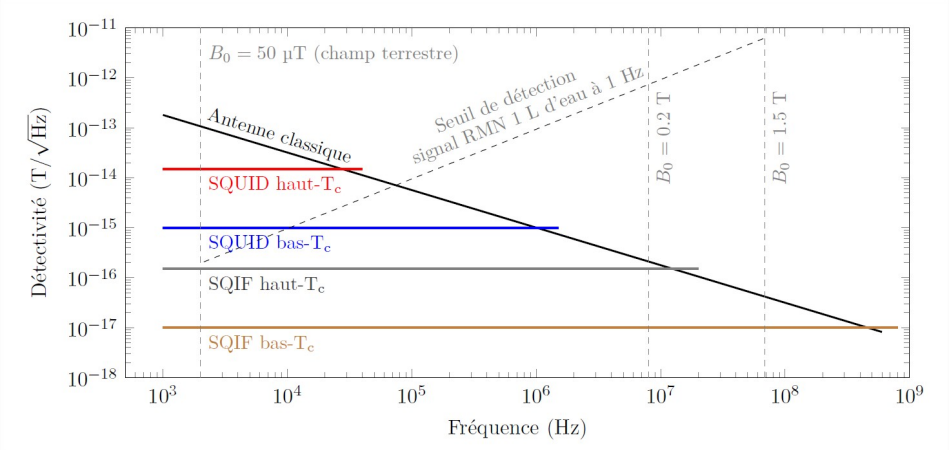

FIG. 3. Detection threshold relative to frequency for various systems. In black you can see that inductive antennas have very low detection threshold for high frequencies, indicating an increase in sensitivity. For frequencies below $\simeq 1$ MHz (corresponding to approx. 25 mT), the SQUID become more sensitive: the blue curve (low T_c single SQUID) crosses the black line of the inductive antenna. Low T_c SQUIDs have typical detection thresholds of a few fT.Hz^{-1} Thesis of Aimé Labbé.

backs that prevent them from being used in a NMR context. Most systems have a narrow bandwidth of a few hundred Hz at most, and they are extremely sensitive to DC inhomogeneous background magnetic fields. Also, OPMs are costly to produce and there is today not enough industrial capacity to scale the production to the industrial level.

- Very low-field MRI has been demonstrated with hybrid magnetoresistive sensors in the team of Claude Fermon [11] [12]. The team has continued developing the sensors while working purely on ultra low field MRI in parallel [13].

- Also, Nitrogen-vacancy (NV) based magnetic detection has been explored as a promising technique for nanometric resolution MRI [14]. NV centers are very small, convenient magnetometers that function at room temperature. They can be placed at the tip of a catheter and are ideal to detect DC or low-frequency magnetism inside the body, or close to a sub-millimetric size room temperature sample. However, their detectivity threshold is at least three orders of magnitude higher than a SQUID, and are thus not useful in our context of macroscopic ultra-low field MRI.

A bit of quantum physics

The SQUID, or superconducting quantum interference device, is a small chip that acts as an extremely sensitive magnetometer, and is at the heart of the ultra-sensitive detection system we are building. The first SQUID was invented at the beginning of the 60's at Ford Labs and Bell Labs. Below we will give a few explanations on where precisely this phenomenon of ultra-sensitive detection comes from.

A typical low-T_c DC SQUID is made out of a small micrometric loop of superconducting material such as Niobium, cooled down to temperatures of order 4 K [15] intercepted by two Josephson Junctions, which are thin insulating barriers that introduce a special kind of quantum interference effect, and allow the SQUID to act as a magnetometer.

So first, let's describe what is a superconductor and how it behaves in a magnetic field.

Current in a superconductor

The reader might remember the basic laws of electrical conduction in a metal, like copper. If you flow an electrical current of intensity I through a copper wire of electrical resistance R, there appears a tension U across the wire such that $U = RI$. This is called Ohm's law, and it describes how a metal wire is "resisting" to the passage of the flow of electrons that make up the electrical current. This resistivity arises, in conventional cases, because of the collision between electrons and small defects, or vibrations (called phonons) of the metallic crystal.

Some materials, like Niobium [16], have a special property that if you cool them below a certain temperature (around 10 K in the case of Niobium), they transit to a *superconducting* state where two things happen:

- The DC resistivity falls to zero,

- The ambient magnetic field is expelled from the bulk of the material, this is also known as Meissner's effect.

These materials are called superconductors. Here is a very handwaving explanation of why this occurs. In the metallic state, electrons are free to move individually to conduct electrical current. At high temperatures, electrons are subject to thermal fluctuations. When you lower the temperature, a very small binding force between electrons appear, because the thermal fluctuations become so small that this binding force starts to take over, and this small force pairs up the electrons together. Individual electrons fall into a category of particle called *fermions*, while pair of electrons are *bosons*, which is the same category of particles as photons, for instance. Bosons have this very special (and nice) tendency to pile up in the exact same quantum state [17]. Because of this, pair of electrons pile up into one single big macroscopic quantum state that has a certain rigidity, meaning that it costs a big amount of energy to escape this state. This big state ignores small defects and vibrations of the metallic crystal, which is why resistivity falls to zero.

Among other things, it directly implies that Ohm's law cannot hold in such systems: in fact, you can have devices with nonzero tension U and nonzero electrical current I with zero electrical resistance. Hence, we need to find a different way to describe electrical current inside a superconductor. This is what the London brothers did in 1935 [18]. Let's assume that in the superconducting state, individual electrons are subject to the classical electromagnetic Lorentz force, $\vec{F} = -e(\vec{E} + \vec{v} \wedge \vec{B})$, where $\vec{E}$ is the electrical field, $\vec{B}$ is magnetic field, e is the absolute value of the electron's charge and $\vec{v}$ the electron's velocity. For nonrelativistic velocities of the electron ($v << c$, c being the velocity of light in vacuum) we can neglect the magnetic term. If we apply Newton's second law to this electron, we find

$$m\frac{d\vec{v}}{dt} = -e\vec{E}. \tag{3}$$

Then we introduce the volumetric supercurrent density [19], defined as $\vec{j} = n_S e\vec{v}$, where n_S is a phenomenological parameter defined by the London brothers as the density of electrons which participate to the superconducting state. This gives the first London equation:

$$\frac{d\vec{j}}{dt} = \frac{n_s e^2}{m}\vec{E}. \tag{4}$$

This gives us information about the time variation of the current. Now, let's take a closer look at the structure of this current. Taking the rotational of the first equation and using Maxwell's equation $\vec{\nabla} \wedge \vec{E} = -\frac{\partial B}{\partial t}$ we get

$$\frac{\partial}{\partial t}\left(\vec{\nabla} \wedge \vec{j} + \frac{n_s e^2}{m}\vec{B}\right) = 0. \tag{5}$$

A superconductor has two fundamental properties: its zero electrical resistance, and another property called the *Meissner effect*, which is that the magnetic field cannot penetrate inside the bulk of the material: $\vec{B} = 0$. Because of Meissner's effect, we immediately see that a constant nonzero solution to the former equation would be nonphysical. Hence,

$$\vec{\nabla} \wedge \vec{j} = -\frac{n_s e^2}{m}\vec{B}. \tag{6}$$

This is the second London equation.

At this point, it is useful to introduce the vector potential $\vec{A}$ through $\vec{B} = \vec{\nabla} \wedge \vec{A}$. As any potential function, much like the potential energy of classical mechanics, it is only defined up to a certain reference. Fixing this reference is called making a choice of *gauge*. In the case of the vector potential $\vec{A}$, because of Maxwell's equations, it is defined up to a vector field of null gradient. We chose the Coulomb gauge, in which $\vec{\nabla}.\vec{A} = 0$. In this gauge [20], the two London equations are nicely summed up into one:

$$\vec{j} = -\frac{n_s e^2}{m}\vec{A}. \tag{7}$$

U(1) symmetry, flux quantization

As discussed previously, electrons in a superconductor all bind into a big macroscopic superconducting state, which is described by a wavefunction $\Psi(r)$ that depends on the position r inside the bulk of the material (in our case, the SQUID). This wavefunction has the property that it is only defined up to a constant phase: the transformation $\Psi \mapsto \Psi e^{i\chi}$, where χ is a real constant, leaves the quantum state invariant. The group associated to this transformation is called $U(1)$ and is a global symmetry [21] of our system.

In most microscopic quantum theories, when you have a global symmetry of your system, it is tempting to assume that it is also *local*, meaning that the phase in the symmetry group depends on the position in space. This "trick" is a lot more profound that it sounds, as it unveils features of the system that were otherwise hidden in the global symmetry. Such local theories are called *gauge* theories, and are the backbone of most modern microscopic theories: quantum electrodynamics, describing light-matter interaction, or quantum chromodynamics / electroweak gauge theory, which make up the Standard Model of particle physics. One very famous manifestation of gauge theory is the emergence of mass through the coupling to a massive scalar field, the Higgs boson. But let's get back to the matter.

Let's assume that the transformation $\Psi(r) \mapsto \Psi e^{i\chi(r)}$ becomes local. The Hamiltonian of the system has a kinetic energy term given by $\frac{(\vec{p}-e\vec{A})^2}{2m}$, where the impulsion $\vec{p}$ is the operator $\vec{p} = i\hbar\vec{\nabla}$. If we want this kinetic term to respect the local symmetry $\Psi(r) \mapsto \Psi e^{i\chi(r)}$, the reader

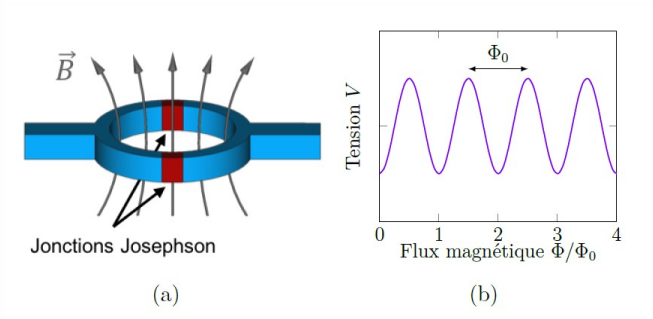

FIG. 4. **(a)** Schematic drawing of a SQUID. **(b)** Voltage-flux characteristic of a SQUID. When a magnetic flux Φ goes through the SQUID, a voltage drop V appears. It varies periodically with flux, with period the flux quantum Φ_0. Measuring this voltage drop V gives access to the magnetic flux Φ, and hence to the magnetic field B we want to measure.

is invited to check that the vector potential field has to transform as

$$\vec{A}(r) \mapsto \vec{A}'(r) = \vec{A}(r) + \frac{\hbar}{e}\vec{\nabla}\chi(r). \tag{8}$$

Now let's define $\phi(r) = 2\chi(r)$ [22].

If we want to respect gauge invariance, the London equation defined in (7) has to be re-written as

$$\vec{j}(r) = \frac{en_s}{2m}\left(\hbar\vec{\nabla}\phi(r) - 2e\vec{A}(r)\right). \tag{9}$$

Now is when we can get to the core of the principle governing a SQUID: the phenomenon of flux quantization.

A SQUID [23] is a small loop made out of superconducting material intercepted by two Josephson Junctions, which are small barriers that split the loop into two parts.

Assume we have a magnetic field B perpendicular to the loop. The flux of the magnetic field going through the SQUID is defined by $\Phi = \int\int_S \vec{B}.d\vec{S}$, where S is the surface of the disk delimited by the SQUID. A supercurrent $\vec{j}(r)$ is induced in the loop by the magnetic field. Let us write the circulation of this supercurrent around the loop:

$$\oint \vec{j}(r).d\vec{l} = \frac{en_s}{2m}\left(\hbar\oint\vec{\nabla}\phi(r).d\vec{l} - 2e\oint\vec{A}(r).d\vec{l}\right). \tag{10}$$

Let's analyse these two terms one by one. The first one gives

$$\oint\vec{\nabla}\phi(r).d\vec{l} = \phi(r)_{\text{after one turn}} - \phi(r). \tag{11}$$

Phase is defined up to an integer number of times 2π:

$$\oint\vec{\nabla}\phi(r).d\vec{l} = 2n\pi. \tag{12}$$

For the second term, we use Stoke's formula:

$$\oint\vec{A}(r).d\vec{l} = \int\int_S \vec{\text{rot}}\vec{A}(r).d\vec{l} = \Phi, \tag{13}$$

which finally gives

$$\oint\vec{j}(r).d\vec{l} = \frac{en_s}{2m}\left(2\hbar n\pi - 2e\Phi\right). \tag{14}$$

In the superconducting state, supercurrents are distributed at the surface of the material. This can be seen as a consequence of Meissner's effect: magnetic field cannot penetrate in the bulk of the material. With this in mind, let's choose a contour C for the integration that passes through the bulk of the SQUID loop, where $\vec{j}_s = 0$ everywhere. We obtain

$$\Phi = n\frac{\hbar}{2e}, \tag{15}$$

where n is an integer. In other words, the magnetic flux going through the SQUID's loop is quantized: it can only take values that are multiples of the flux quantum, $\Phi_0 = \frac{\hbar}{2e}$.

What we learn from this is that when a magnetic field goes through the loop of the SQUID with a flux Φ, the SQUID will react by generating a small current I. This current creates a small counter-flux $\delta\Phi$ that will re-establish the total flux to the nearest-integer multiple of Φ_0:

$$\Phi_{tot} = \Phi - \delta\Phi = n\Phi_0. \tag{16}$$

To exploit this phenomenon, we will add another ingredient to our superconducting loop: two Josephson Junctions in parallel, as described in fig. 4. We won't go too much into the details of the physics of Josephson Junctions as it would be a bit too heavy for this introductory white paper. A very good description of Josephson equations in a SQUID is done in the PhD thesis of Nazim Lechéa (part. III.1) [24], if you read french. Also, another very good reference is the book of John Clarke (part 2.1.) [25]. Below we give the main ideas behind the reading of a magnetic field by the SQUID.

In the presence of the two junctions, the current circulating in the loop is given by

$$I(\delta) = I_0\sin(\delta), \tag{17}$$

where I_0 is the critical current of the junction, and δ represents the total dephasing of the system's wavefunction across the junctions. It is given by $\delta = \Delta\phi_b + \Delta\Phi_{mag}$, where $\Delta\phi_b$ is the "bare" dephasing of the wavefunction without the presence of the magnetic field, and $\Delta\Phi_{mag} = 2\pi\Phi_a/\Phi_0$ the dephasing due to the magnetic flux Φ_a going through the loop. This equation is the first Josephson equation and describes the system well for small current intensities $I < I_0$. What's more interesting is to pre-bias the system to a current close to I_0. When the current generated by the magnetic flux goes above this limit, a tension U_j appears across one junction, given by

$$U_j = \frac{\Phi_0}{2\pi}\frac{d\delta(t)}{dt}, \tag{18}$$

which is the second Josephson equation. Solving this couple of equations for the whole system, we get that the tension $U(\Phi_a)$ across the SQUID varies periodically with the applied magnetic flux Φ_a, in the form

$$U(\Phi_a) = U_0 \sin(2\pi\Phi_a/\Phi_0). \tag{19}$$

For small amplitudes of flux, which is what the SQUID is designed to measure, close to a point of highest slope, the variation of tension ΔU is linearly linked to the variation of magnetic flux $\Delta\Phi$ via

$$\Delta U = 2\pi U_0 \frac{\Delta\Phi}{\Phi_0}. \tag{20}$$

For very low fields in the pT range, this tension can be of order of a few μV. It then gets amplified by low temperature preamps to reach a few V in room temperature electronics. This makes SQUIDs extremely sensitive magnetometers, with noise levels in the $\mathrm{fT}/\sqrt{\mathrm{Hz}}$ range.

What a SQUID detection system looks like

A typical MRI detection system based on SQUIDs is always constituted of a few core parts:

- A flux concentrator, whose job is to concentrate the magnetic signal towards the SQUID,
- One or several SQUIDs, who read the incident signal,
- A low-temperature preamplification system,
- Room-temperature electronics to make analog-to-digital conversion and feedback to ensure stability of the SQUID system.

I will say a few words about the first element, the flux concentrator, which is highly critical regarding the sensitivity of the whole system. A SQUID can be imagined as a small ring made out of superconducting material, intercepted by two "barriers" called Josephson junctions, with diameter in the μm range. Because of its small size, the SQUID intercepts only a tiny fraction of the signal sent out by the sample. A common way to circumvent this issue is to couple the SQUID to a *flux concentrator*. It is just a common loop antenna, called the *pickup coil* in series with an *input coil* which is a small coil that sends the captured flux through the SQUID. You can think of it as the pickup coil capturing the signal and sending it to the SQUID that reads it.

A very thorough explanation on the different types of flux concentrators that one can use has been done by Fagaly [26]. There are two important parameters to choose when designing the pickup coil: its geometry, and the nature of the wire you're going to use. Usually, coils fall into two geometrical categories: surface or volume coils. Surface coils are often smaller and allow minimal intrinsic noise, and also allow to design *gradiometric* geometries that reject far-field noise. The trick is to split the antenna into two parts that run against each other. Objects close to the antenna send out signal that will get detected, but noise from faraway sources induces the same signal into the two parts of the antenna. As a consequence signal in the two parts compensate one other, and the resulting signal averages to zero.

Volume coils have been less explored in the context of SQUID MRI but they are standard in the case of classical inductive MRI, where saddle-coil or birdcage geometries are often used [27].

Regarding wire, you have the choice between a classical ohmic conductor such as copper or a low-temperature superconductor, Niobium wire being a standard. Copper wire has the advantage to be able to operate at any temperature, at the expense of producing more Johnson-Nyquist noise. This voltage noise goes as $\Delta u = \sqrt{4k_B T R \Delta f}$, where k_B is Boltzmann's constant, T is temperature, R is the wire's DC resistance and Δf is the bandwidth over which you're measuring the noise. To minimize this noise, it is a good idea to choose high-quality OFHC copper that has a very low resistivity, and to cool down the antenna, for instance in liquid Nitrogen. Niobium wire, on the other hand, is a superconductor and has to be cooled down below 10 K to be used. Because of this, a niobium pickup coil has to stay at the heart of the cryostat, far away from the object you need to measure, and only a handful of surface geometries can be used. Of course, the Johnson noise is going to be a lot less in a Niobium wire. Hence, choosing copper or niobium wire will be a trade-off between flexibility on the geometry of the coil, and minimizing the intrinsic Johnson noise of the antenna.

Until now, most low-T_c SQUID-detected MRI systems have used superconducting second-order axial gradiometers, see eg. Zotev et al. 2007 [28] or Penanen et al. 2014 [29]. Some high-T_c experiments have used ohmic volume antennas, such as the device of Chen et al. 2011 [30]. At Chipiron, we believe that the geometry of this primary antenna is the key to increase the SNR enough to be able to perform SQUID MRI in a clinical setting. We'll develop this point further in the next part.

THE CHIPIRON APPROACH TO SQUID MRI

Current state of research

20 years of ultra-low field MRI

SQUID-detected MRI, or more generally ultra-low field MRI, is not a new topic. The first research on the topic was conducted 20 years ago in the team of John Clarke in

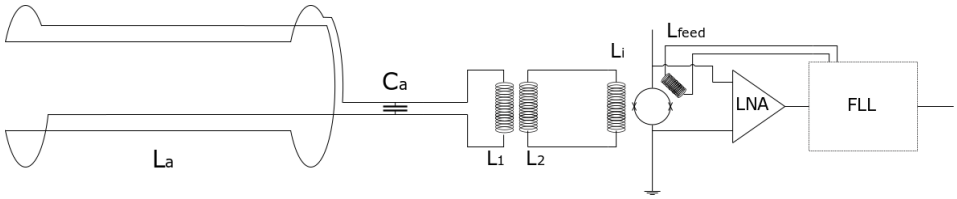

FIG. 5. A simplified view of a typical SQUID detection system for an MRI experiment. On the left is the primary antenna, a resonant saddle coil in this example, that captures the signal to send it to the SQUID loop (in the middle of the picture, circle with two crosses, which represent the Josephson Junctions). The SQUID reads the signal, and its output is amplified by a low-temperature cryogenic preamplification system. Then, the signal is sent to room-temperature electronics which ensure amplification, feedback, and analog-to-digital conversion.

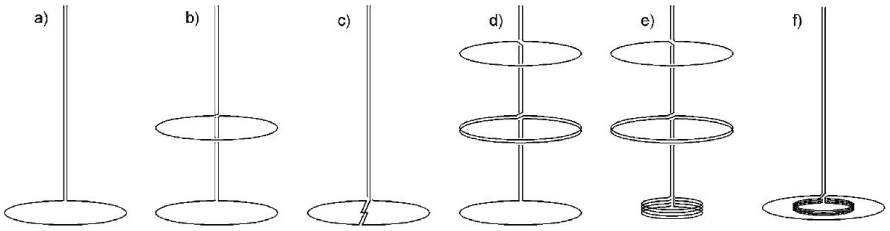

FIG. 19. (a) Magnetometer; (b) first derivative axial gradiometer; (c) first derivative planar gradiometer; (d) second derivative axial gradiometer; (e) second derivative asymmetric axial gradiometer; (f) first derivative radial gradiometer.

FIG. 6. A few examples of geometries for surface antennas. Apart from antenna a), all other geometries are of gradiometric nature: the several coil turns compensate each other. If you call b the distance between two of the loops, signal sent from distances of order b or less will get detected. On the contrary, if the emitting object lies at a distance $>> b$, the different coils compensate each other and the resulting signal is zero. Sketches from b) to f) present several alternatives of gradiometers of different orders and different geometries. The higher the order, the most effective you are at rejecting faraway noise but the less sensitive you become. Fagaly et al., 2006.

Berkeley [31],and got developed in parallel in the team of Michelle Espy at Los Alamos, with applications towards a hybrid MEG/MRI system [32]. In all SQUID MRI experiments up until now, the strategy is to use a technique called pre-polarization. The idea is to first apply a moderately high magnetic field for a few seconds, usually around 100 mT, to pre-polarize the sample. As equilibrium polarization increases linearly with the applied field, at 100 mT, you have 1000 times more polarized protons than at 100 μT, leading to a factor 1000 increase in the available signal. Once your sample has reached its equilibrium polarization, you quickly lower the field to the measurement value, around 100 μT in the case of SQUID MRI, and the MRI sequence is then performed at this ultra-low field. Doing the actual MRI at an ultra-low field instead of 100 mT has two main advantages. First, the field homogeneity is a lot better, leading to less artifacts. In fact, what matters in the context of NMR is to have a good value for the *absolute* field homogeneity, while the geometry of the polarization coil imposes constraints on the *relative* one. This means that a good absolute field homogeneity is easier to get at low fields than at high fields. A good ballpark figure for the absolute field homogeneity required over the whole field of view would be $\Delta B_0 \simeq 100$ nT. This would mean that the spectral broadening due to inhomogeneities $\gamma \Delta B_0$ is of the same order of magnitude as $1/T_2$. For a magnet of $B_0 = 1$ mT, this translates into a 100 ppm relative homogeneity, which is not too hard to achieve with a set of large Helmholtz coils, keeping an open geometry. At $B_0 = 3$ T, this is a 0.03 ppm requirement, which imposes a closed bore geometry and careful shimming of the magnet. Secondly, and most importantly, the contrasts (notably T_1 contrast) are much higher, allowing to produce new images and eventually open new clinical applications. In short, pre-polarized ultra-low field SQUID MRI allows to take advantage of both the upsides of high field (more signal) and low field (portability, better contrast, better homogeneity).

Obviously, this technique does not come without drawbacks, and we don't think this strategy is the most relevant. First, the prepolarization phase takes a lot of time in the MRI experiment. Secondly, the heavy machinery used to pre-polarise the sample hinders the transportability of the device and generates electromagnetic noise because of eddy currents caused by the rapidly varying magnetic fields. Taking the paper of Espy, 2015 [33] as an example, the pre-polarization phase takes a time $t_p = 4$ s, and ramping down the field from 100 mT to the measurement field (200 μT in this case) takes $t_r = 100$ ms. Then the actual MRI sequence can begin, with a phase encoding step of 35 ms, and a readout phase taking 70

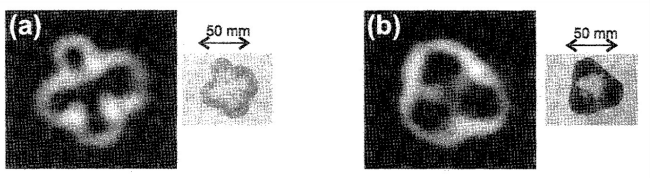

FIG. 7. One of the first SQUID MRI acquisition (2004): image of the inside of a bell pepper obtained with SQUID-MRI at 132 μT with prepolarization at 300 mT. Image (a) corresponds to a 2D acquisition sequence while image (b) is a cut from a 3D sequence. Images are acquired with a spin-echo sequence in 5 mins with an in-plane resolution of about 1 mm. McDermott et al., 2004.

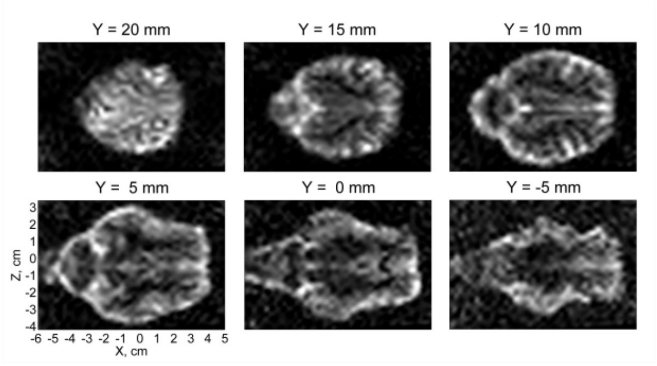

FIG. 8. An improved SQUID MRI experiment (2007): T2-weighted MRI images of a sheep brain acquired at a field of 46 μT, using a multi-channel low-T_c SQUID detector with prepolarization. Different Y values correspond to different cuts of the brain in the vertical plane. The in-plane resolution is 2.5 mm x 2.5 mm, with multiple acquisitions and averaging, for a total scan time of 3 hours. Zotev et al., 2007 [28].

ms, for a total sequence duration $t_s = 100$ ms. This means that, for one repetition, the prepolarization time $t_p + t_r$ accounts for about 97.5% of the total acquisition time $t_p + t_r + t_s$. However, if we make the very optimistic assumption that the pre-polarization scheme doesn't add noise compared to the 200 μT sequence with no prepolarization, then the prepolarization increases SNR by a factor 500. Taking into account the factor of 40 due to pre-polarization time, this scheme increases SNR by unit time by a (very sizeable) factor of 12.5. This is the reason why pre-polarization techniques have been so popular in the field of SQUID MRI. It is however to be noted that doing no-prepolarization while increasing the measurement field by a factor of 12.5, which would be doing MRI at 2.5 mT, would in theory provide the same range of SNR increase with the advantage of using no cumbersome pre-polarization.

Now let's consider the detection system. Most of the time, the antenna used for detection is a low-T_c SQUID in conjunction with, as a flux concentrator, a superconducting second-order gradiometer made out of Niobium wire. This particular configuration is useful for several reasons. Firstly, the use of superconducting wire allows for a very low electrical resistance, limiting Johnson noise. Secondly, the second-order gradiometer configuration makes the device insensitive to noise coming for faraway sources, as was pointed out by Fagaly et al [26]. The second order gradiometer is a sweet spot in antenna design: a first order gradiometer is a bit more sensitive but remains fragile towards noise, while third and higher orders become too insensitive to the signal of interest with little improvement in noise rejection.

The axial gradiometer configuration also allows to easily configure a multi-channel system that can be used to perform an MRI experiment in conjunction with a MEG experiment. This is the idea presented in the paper of Zotev et al. [28], and is a subject of intense development in the Brain imaging group at the Aalto university [34]. A hybrid MEG/MRI system, even operating in a heavily shielded room, would be an extraordinary tool for neuroscience experiments.

Since the early days, a lot of effort has been done to try to improve image quality and acquisition time, as well as to design even lighter experiments. A very thorough and in-depth picture of the landscape of SQUID-powered low-field MRI can be found in a recent review from Sarracanie and Salameh [35]. Some of the most recent results in-vivo include the paper of Clarke, 2013 [36] where brain images were acquired in 26 minutes at 130 μT (prepolarized at 80 mT) with in plane resolution of 2.5 x 1.9 mm and 100 mm thick slices. The team of Espy, 2015 [33] also got brain images in 67 minutes at 200 μT (prepolarized at 100 mT) with in plane resolution of 2.1 x 2.4 mm and 150 mm thick slices.

The work of Kawagoe as well as Demachi, fig. 9, aims to build a SQUID-powered MRI machine for food inspection. These experiments use high-T_c SQUIDs with Copper flux transformers, that require a very light cryogenic system based on liquid nitrogen, which is an advantage compared to their low-T_c counterpart. The results show promising images for their specific applications in food quality control, yet remain outside the standards needed for clinical imaging. The paper of Liu et al. 9 presents a very useful active compensation technique designed to compensate for DC fluctuations of the polarization field in the case of traditional low-T_c second-order gradiometric SQUID MRI. This type of technique will be of a big interest for our product if we want to operate in an open noisy environment such as a hospital room or an ambulance. Very recently in March 2023, the team of Oyama et al. developed a 1 mT SQUID MRI/MEG device with no prepolarization [37], which is the closest to the Chipiron machine it gets. The device operates in a magnetically shielded room and is projected to be used in conjuction with MEG, like most SQUID MRI previous

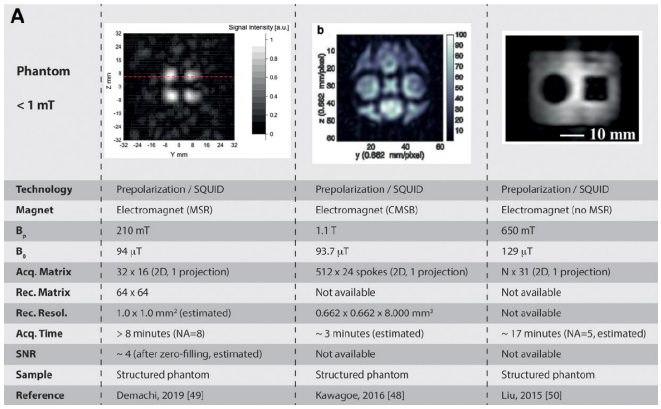

Technology	Prepolarization / SQUID	Prepolarization / SQUID	Prepolarization / SQUID
Magnet	Electromagnet (MSR)	Electromagnet (CMSB)	Electromagnet (no MSR)
B_p	210 mT	1.1 T	650 mT
B_s	94 μT	93.7 μT	129 μT
Acq. Matrix	32 x 16 (2D, 1 projection)	512 x 24 spokes (2D, 1 projection)	N x 31 (2D, 1 projection)
Rec. Matrix	64 x 64	Not available	Not available
Rec. Resol.	1.0 x 1.0 mm² (estimated)	0.662 x 0.662 x 8.000 mm³	Not available
Acq. Time	> 8 minutes (NA=8)	~ 3 minutes (estimated)	~ 17 minutes (NA=5, estimated)
SNR	~ 4 (after zero-filling, estimated)	Not available	Not available
Sample	Structured phantom	Structured phantom	Structured phantom
Reference	Demachi, 2019 [49]	Kawagoe, 2016 [48]	Liu, 2015 [50]

FIG. 9. Recent phantom images (not in-vivo) from the last 5 years obtained in SQUID-detected MRI. Fields are all in the range of 100 μT with prepolarization, with millimetric resolution and acquisition time of 8, 3, and 17 minutes, respectively. Excerpt from Sarracanie et al., 2020, original works are from Demachi et al. [c], Kawagoe et al. [c], Liu et al. [c]

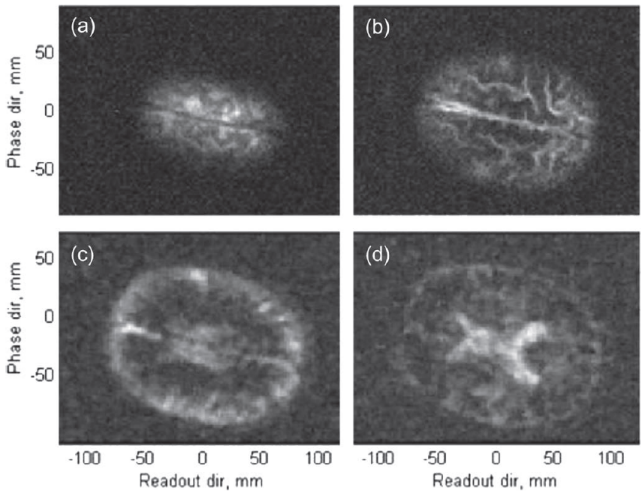

FIG. 10. One of the most recent in-vivo pre-polarized SQUID experiments in the team of Los Alamos (2015). Brain images were acquired in 67 minutes at 200 μT (prepolarized at 100 mT) with in plane resolution of 2.1 x 2.4 mm and 150 mm thick slices. Several (axial) slices are shown, the SNR of the images is ~ 10.

[a] K. Demachi, et al., IEEE Transactions on Applied Superconductivity **29**, no. 5, 1-5, (2019).
[b] S. Kawagoe et al., Physica C: Superconductivity and its applications **000** 1-5(2016).
[c] C. Liu et al., Journal of Magnetic Resonance **257** 8-14(2015).

attempts. This experiment that bears a lot of technological similarities with ours validates that we are going in the right direction. While the SQUID is a very powerful tool to detect the NMR signal at ultra low-fields, some teams have also been using conventional inductive detection, the most notable example being the team of Matt Rosen at the Martinos Center, working at 6.5 mT with b-SSFP sequences, as shown in fig. 13.

Contrasts at low fields

Let's take a look at the theory behind the possible improvement of contrasts at ultralow fields with a simplified model. Considering two voxels made from two tissues A and B, and the signal received from them S_A and S_B, we define the contrast $C_{A,B}$ as simply

$$C_{A,B} = S_A - S_B. \tag{21}$$

Note that we just take this as an example, it is possible to argue that one should normalise this equation either by the amplitude of the signal or even the noise (which defines the Contrast to Noise Ratio CNR). The goal of the following paragraph is to illustrate the mechanism that makes an increase of contrast possible. In a typical spin echo sequence with only T_1 contrast (the calculation is very similar for T_2^* or T_2 contrast), the signal decays exponentially as

$$S_A \propto e^{-T_R/T_1^A} \tag{22}$$

where T_R is the repetition time. Looking at the equation of the contrast, it is mainly dependent on the difference of decay rates

$$\left| \frac{1}{T_1^A} - \frac{1}{T_1^B} \right|. \tag{23}$$

The larger this quantity, the easier it will be to distinguish the two tissues since it will possible to find an appropriate echo time T_R to measure a significant gap between the two signals. A proper analysis takes into account the normalisation, the difference of density or even the flip angle. Low field-MRI can provide a better contrast if this difference of decay rates increases at low field. From relaxation theory [38], one can find that the relaxation rate $1/T_1$ depends on the magnetic in the following way

$$\frac{1}{T_1} = \frac{2K\tau_c}{1+(\omega\tau_c)^2} + \frac{8K\tau_c}{1+(2\omega\tau_c)^2} \tag{24}$$

where ω is the Larmor frequency (directly proportional to the magnetic field), τ_c is the tumbling rate related to the correlation time of the magnetic perturbation due to the spin in the structure, and K is a constant related in particular to the density of the tissue. This equation is a simplified model of how relaxation works in tissues, it is however useful for pedagogical reasons and to provide general criteria. By looking at the difference of T_1 between two tissues, one can argue that low field contrast would be improved in particular for pair of tissues where one is both denser and stiffer than the second one. However there are no absolute theoretical rules, we will

produce experimental data at ultra low fields to draw definitive conclusions. The increase in T_1 contrast has been already been demonstrated at low fields in the specific case of prostate cancer screening.

Current strategy and its limitations

The progress made in the past few years gives us a lot of evidence that SQUID-powered clinical MRI is about to be a reality. The drastic decrease of acquisition time and gain in resolution presented in the last works is going in this direction. However, the big problem is that the signal-to-noise ratio (SNR) is still too poor, usually of order 1 to 10, preventing to obtain good resolution with no artifacts in reasonable time. Below we detail what are the key components used in most existing SQUID MRI experiments, and what challenges do they introduce.

1. **Prepolarization.** The ultra-low field used in most experiments, around 100 μT, is too low to hope to make a clinically relevant MRI acquisition in reasonable time. Most experiments done at this range of field exploit a technique called prepolarization where you first polarize the sample at a field of order 10 to 100 mT and you then quickly lower the field at 100 μT to perform the MRI sequence. As we pointed out earlier, this pre-polarization scheme takes more than 95% of the time in the MRI sequence. Also, the rapid switches in pre-polarization field from a few mT to 100 μT create eddy currents that add a lot of noise to the experiment. We believe that it would be best to work at higher fields, that would allow for more signal without the need for pre-polarization. The measures of Lee et al. [39] show that there is still some room for higher fields that still allow for the great enhancement of T_1 contrast permitted by the low-field regime.

2. **Shielding.** As was pointed out in the review of Sarracanie [35], most SQUID MRI experiments are performed in magnetically shielded rooms (MSR), the reason being that it lowers by orders of magnitude the environmental noise and improves SNR as a consequence. These rooms are usually built with a few-mm thick Al or Cu plates covering the walls, acting as a Faraday cage, sometimes adding layers of magnetic materials such as ferrites or mu-metal to suppress low frequency components of the noise. This type of setting is ideal for an MRI experiment but reproduces the pain associated with high-field machines: an MSR suitable for a clinical setting is very expensive, typically in the \$10k - \$100k bracket, and obviously not transportable. It is a great challenge to overcome this constraint to work in an open noisy environment. We want to design an open MRI machine, that can work in any environment, a normal hospital room, the doctor's office, or even an ambulance truck. These type of environments are very noisy, but as we will detail later, some light, inexpensive active forms of shielding can be used.

3. **Geometry of the antenna.** The usual flux concentrator for the SQUID pickup coil of MRI experiments is a second-order surface gradiometer made out of Niobium wire. This geometry is chosen because it is a good compromise between sensitivity and robustness to noise. Very few other geometry candidates have been explored, one of the reasons being that a lot of SQUID-MRI experiments focus on a hybrid device that performs a MEG experiment on top of the MRI [40] [28]. This could have game-changing implications in the field of neuroimaging. This approach, however, imposes great constraints on the precise position of the different SQUID channels, as well as the geometry of the flux concentrator. This type of approach does not allow for a lot of exploration in geometries, which we believe is crucial for clinical SQUID MRI.

4. **High-T_c or low-T_c.** A lot of attention has been given recently on the potential of high-T_c SQUIDs for NMR and MRI. Devices like those of Sustera [41], in Japan, can have detectivity thresholds as low as 10 fT.Hz$^{-1/2}$. The promise of high-T_c cuprates for SQUID MRI is big, as it could greatly reduce cost and ease of use because of the requirements of low-T_c cryogeny. High-T_c materials only requires light cryostats and liquid Nitrogen which is cheap and accessible. However, because of their intrinsic thermal noise that is a lot greater at 77 K than it is at 4 K, the ideal detection threshold of about 0.1 fT.Hz$^{-1/2}$ is going to be a lot more challenging to reach than with the low-T_c devices. Moreover, and most crucially, high-T_c ceramics are extremely hard to engineer. It is notoriously challenging to build reproducible, clean Josephson Junctions in cuprates. SQUIDs contain two Josephson junctions, and small asymmetries can quickly degrade performance. Also, array of tightly controlled high-T_c SQUIDs will be hard to design, even in a very controlled laboratory setting, let alone at the industrial scale, even if some promising technologies have emerged in the past few years [42].

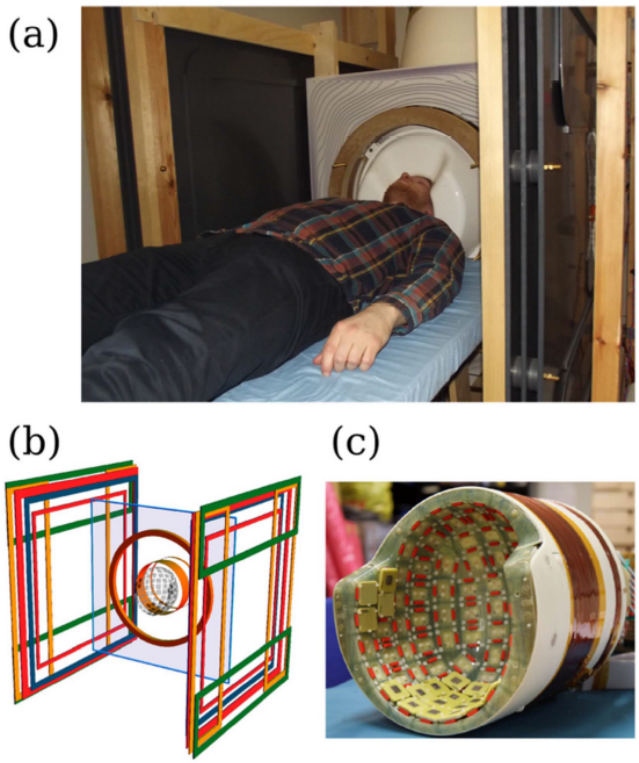

FIG. 11. The LRI-MEG system of the team at Aalto university. (a) General outlay of the experiment. (b) Configuration of the gradient, polarization, and excitation coils. (c) MEG-MRI helmet with all the sensors. [34]

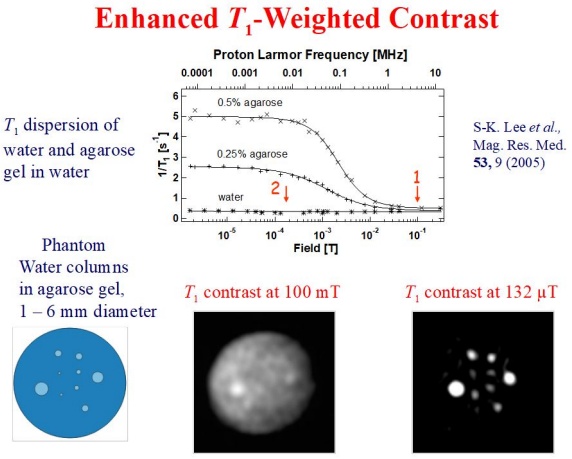

FIG. 12. Evolution of T1 contrast with magnetic field. Below about a few mT, T1 contrast is greatly enhanced, here on the example of a solution containing different concentrations of agarose. This property allows for the design of special T1-weighted sequences particularly suited to low-field MRI. [38]

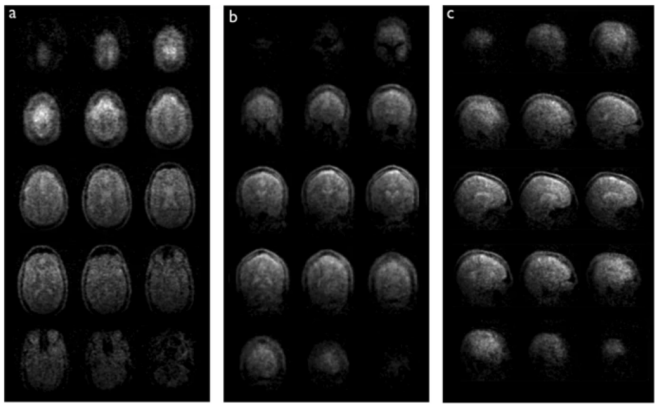

FIG. 13. In-vivo 3D images of a human brain acquired with a b-SSFP sequence in 6 minutes at 6.5 mT in (a) axial, (b) coronal and (c) sagittal orientation. The corresponding maximum SNRs are a. 15, b. 21 and c. 16. Acquisition matrix: 64∗75∗15, voxel size: A. (2.5∗3.5∗8.5) mm^3, b. (2.5∗3.5∗11.5) mm^3, and c. $(2.5 * 3.5 * 14.4)$ mm^3. [42]

How we are going to make a difference

Key technological developments

Taking into account all these challenges, we designed a strategy to improve each point of the experiment, from the detection system to the full MRI device. We started the experiments in July 2021, for now most of the strategy is at the exploration stage, results will be added to this publication as they come. Most of our work is still awaiting patent publications, hence we will not give too much details in this last part. We just want to give you a general overview of our strategy to foster discussions.

1. **A novel antenna geometry.** We think that finding specific pickup coil designs for precise clinical applications will be a game-changer in SQUID MRI. For the past two years we have been working on a gradiometric volume coil that has the potential to lower the detectivity threshold of the SQUID detector by up to one order of magnitude, operating in a open environment. Two patents have been filed on this antenna, the first one being published during the summer of 2022. To try to gauge the ballpark of image quality we can reach with our detection system, let's go back to the discussion about SNR in the part about the history of SQUID MRI. Doing MRI with no prepolarization and with the same usual surface gradiometer pickup coil would require in theory a field of order 10 mT to match a prepolarized experiment in terms of SNR, which lies somewhere between 1 and 10 in most SQUID MRI experiments. Taking into account the fact that prepolarization adds sizeable noise, this figure could in fact be a bit lower, in the range of a

few mT. We call this field the crossover field B_c and we'll take $B_c = 5$ mT for our discussions. Our first results seem to indicate an increase of SNR between 5 and 10 with our new geometry, so let us assume we can reach a SNR of 30 working at a field between 1 and 3 mT. What kind of images can we get with such SNR? A good point of reference is the work from the team of Matt Rosen [43], where brain images with resolution 2.5 x 3.5 mm and 8.5 mm thick slices have been produced at non-prepolarized 6.5 mT with SNR ranging between 15 to 25, with acquisition times of around 6 minutes. This experiment shows that ULF images with reasonable SNR are possible in clinically relevant time of acquisition. We plan to go further with increased SNR and contrasts thanks to an even lower field, and most importantly in an open unshielded setting. Our first results in the first half of 2023 confirmed these estimates, we are waiting for the first images by the end of 2023, which will be improved to reach clinical relevance by the end of 2024.

2. **Ultra-low field.** One big advantage compared to our competitors working at low field, such as Hyperfine (who work at 64 mT), is the increase of contrasts one can get at 1 mT. Better contrasts, especially T_1 contrasts, mean better diagnosis power for a lot of pathologies, even if the resolution is not on par with the high field technology. This fact is well explained in fig. 12 on a simple example of water and agarose gels. In our opinion, the sweet spot for contrast increase while retaining enough SNR lies around 500 μT to a few mT. Some target applications that can greatly benefit from a small, inexpensive MRI device with increased T_1 contrasts include emergency traumatology of extremities (knee, ankle, wrist), screening for prostate cancer [44], or endometriosis (particularly Deeply Infiltrating Endometriosis, or DIE) [45], as well as interventional neuroradiology. In the case of endometriosis, the meta-analysis of Tong et al. shows that a light MRI solution could show great benefit for screening, mostly in the case of DIE where ultrasound diagnosis relies too much on the skill of the operator and patient-dependent factors.

3. **Open geometry, transportable.** It is a key point for MRI accessibility to keep the design very light and open. Light, because it allows the machine to be easily transported from one point to another, which is essential for emergency applications or for use in a point-of-care setting or a local doctor's office. Open, because it increases patient comfort and unlocks the use of MRI for patients suffering from obesity or claustrophobia. Also, it would drastically reduce the use of anesthesiant drugs on children with anxiety and allow the parents to stay close to their children during the whole examination. MRI is following the same route as ultrasound technology did twenty years ago: a new branch of open, transportable MRI is emerging for easy, inexpensive, and effective diagnosis. Our light excitation-detection system is comprised of the primary antenna, a radiofrequency excitation coil, and a resistive polarization coil, all combined into one piece that can be brought close to the zone of interest. The cryostat containing the SQUID and readout electronics, the gradient and RF amplifiers, and the analog-to-digital conversion will be placed in a separate part which communicates with the excitation-detection antenna. This configuration allows for maximum patient comfort and minimum vulnerability to magnetic noise.

4. **Active shielding (no MSR).** We want to be able to operate in an open environment, so a fully magnetically shielded room, or a Faraday cage are both out of the question. Our strategy is to design a light shielding system that uses active noise cancellation/substraction. In fact, after a few months of design and exploration, we came to the conclusion that passive shielding techniques, even if semi-open, are too heavy to allow for a transportable machine. A full Faraday cage for the machine, made out of a few mm thick Cu and Al plates would easily weigh in the hundreds of kilograms and raise the size of the machine to a few cubic meters. Also, DC shielding composed of ferrites or mu-metal are even more heavy, expensive, and very fragile. On the other hand, active compensation techniques have recently proven to be extremely effective in the framework of low or ultralow field MRI. For instance, Liu et al. 9 designed a technique to compensate for polarization field fluctuations to retain the needed magnetic field stability and homogeneity during the sequence. On the topic of RF noise cancellation, the team of Ed X. Wu designed a 55 mT brain scan MRI that works with a cancellation technique based on deep learning which can accurately predict and substract the noise [46]. Their results are displayed in fig. 14. We plan to implement such techniques, as well as real-time noise cancellation techniques which could be suitable in our case given the relatively low frequency of work of a few tens of kHz. We are lucky enough to have experts in active shielding who are permanent researchers in our lab in Paris.

5. **Rapid low field MRI sequences.** Working at ultra-low fields is in the common wisdom often synonym of very low signal-to-noise ratio, poor image quality, and long acquisition times. This has proven to be less and less true in the past few years as tremendous efforts have been made

to design rapid MRI sequences that use partial sampling, image reconstruction, and clever exploration of the k-space. Some examples of post-treatment include the method of *backprojection* at ultralow fields of Xiaodong Yang et al. [47] or the SPARKLING method developed by Carole Lazarus and Philippe Ciuciu [48]. Regarding sequences, the team of Rosen at the Martinos center has made good use of Steady state free precession (SSFP) type of sequences, mostly balanced SSFP, that have amongst the highest rates of SNR per unit time of sequence, particularly adapted to ultralow fields. In the same fashion, quantitative imaging techniques such as Magnetic resonance fingerprinting [49] has surged a lot of interest recently [50] and could be a huge opportunity to complement traditional high-field MRI, for instance in the case of prostate cancer screening [51]. Given the long times of acquisition at low fields, combining quantitative maps to generate synthetic contrasts is also a promising route. Most importantly, we collaborate with experts of low-field sequences, Eric Thiaudière and Elodie Parzy of the Université de Bordeaux [52] [53] [54] [55]. In this collaboration, we are currently designing sequences that take full advantage of the precious T1 contrast that can be obtained at low fields, while keeping acquisition time in an acceptable range of 5 to 8 minutes with close to millimetric spatial resolution.

6. **Low T_c SQUIDs.** To keep the technological risk at a minimum, we started working with the low-T_c SQUID devices of STAR Cryoelectronics [6]. These devices have the advantage of being very effective in terms of intrinsic noise and shielding, while being easy to set up in our MRI experiment. We also firmly believe that high-T_c SQUIDs for MRI is too early of a topic for now. Long-term, we plan to fabricate our own SQUID devices in collaboration with the dense ecosystem of clean rooms and microfabrication facilities in the heart of Paris, close to our lab at the ESPCI. Low-T_c is often associated with lack of portability, either because of the cumbersome procedure of liquid He filling and recycling, or because of the heavy cryocooling system. In our case, we are designing a light low-power cryostat with a dedicated low consumption pulse-tube cryocooler that provides 10 mW at 4 K, for a power consumption of less than 1 kW and taking up no more than 4 - 5 rack units.

Research axes

Given these core development topics, our long-term strategy includes a sizeable part of research. Here are some key topics that will constitute the technological backbone of continuous improvement of our detection performances, as well as opening opportunities for novel applications.

1. **Powerful low temperature amplification systems.** The output signal of the SQUID, a tension of order a few μV, needs to be amplified to a few V for signal treatment and analog-to-digital conversion. The readout electronics also include a feedback loop that maintains the SQUID at a point of maximum sensitivity. If we want to take advantage of the extraordinary performances of the SQUID, these electronics need to have a very low input noise level not to degrade the signal-to-noise ratio. In most cases, apart from the pre-amplification stage, all the electronics lie at room temperature and amplifier input noise is in the range of 1 nV/$\sqrt{\text{Hz}}$. There is an interest to develop electronics fully operating at 4 K to quantitatively improve input noise performances. Our collaborators at laboratoire APC - Université de Paris are developing cold, ultra-low noise electronics for SQUID readout [56]. Their main application is the readout of multiplexed TES (transition edge sensors), which are superconducting bolometers used in the QUBIC experiment, aiming to measure the polarization distribution of the Cosmic Microwave Background. We are currently working to integrate this technology into custom readout electronics.

2. **One or many SQUIDs?** SQUID networks have been an active topic of research since the late 90s. Imagine you have a network of N identical SQUIDs in series that feel the same magnetic flux Φ. At least in theory, if all the detectors are in phase, the total voltage drop across the N SQUIDs will be the sum of all individual in-phase voltages, making the maximum sensitivity of the system $\partial V/\partial\Phi$ N times higher than the sensitivity of one individual detector. This is a case of constructive quantum interferences. In practice, things are not so simple. If detectors are all independent, the noise sums up in the chain as $\sqrt{N}$ and sensitivity only grows as $\sqrt{N}$. Taking into account screening, this figure in fact saturates quickly as the chain grows. Also, the $V(\Phi)$ characteristic remains non-linear in an identical multi-SQUID chain, which needs adapted feedback electronics for a multi-SQUID system. This problem has been famously circumvented with the discovery of SQIFs (superconducting quantum detection filters), which are non-identical SQUID chains with special surface distribution. These SQIFs allow to have a non-linear characteristic with a broad antipeak around $\Phi = 0$, allowing operation without a feedback loop, which implies a greater

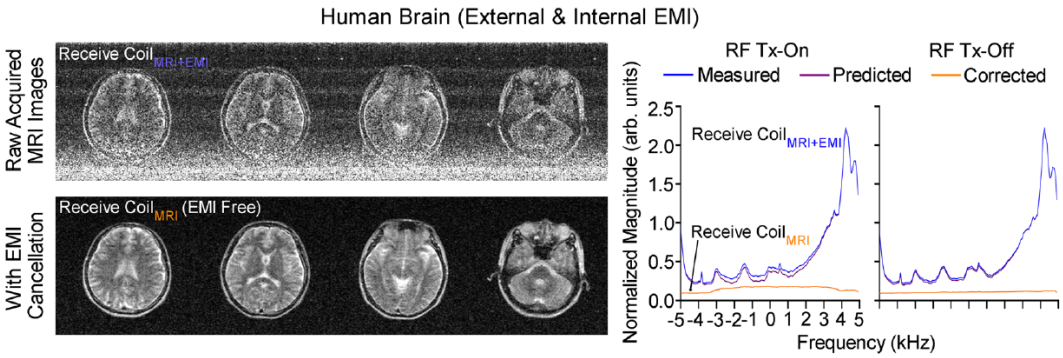

FIG. 14. Deep learning-driven noise cancellation in a T_2-weighted 55 mT brain scan. On the left, the result of the acquisition with our without the cancellation technique applied. On the right, The amplitude of the signal in arbitrary units with or without the activation of the transmit RF channel. The algorithm-predicted signal (in purple) matches very well the measured signal (in blue) and allows for correction of the RF noise, which gives the clean corrected signal (in orange). [45]

dynamical range and the possibility to work at ultrahigh frequencies. These systems have been successfully implemented with high-T_c SQUIDs by our collaborators at ESPCI [57]. Whether in identical or non-identical chains, we will have to find a way to properly couple our flux concentrator to the chain of SQUIDs such as every detector is in phase with one another, while keeping the geometry carefully controlled and the noise minimal.

3. **Higher temperature SQUIDs for more efficient cryogeny.** As we previously pointed out a couple times, we believe that despite some promising recent advances, high-T_c SQUIDs for MRI remains to this day too challenging of a topic for commercial use in the foreseeable future for two main reasons: the high level of thermal noise due to higher temperatures and the difficulty to fabricate ceramic Josephson junctions in a convenient, reproducible fashion. However, if we put aside the high-T_c cuprates, another higher temperature superconductor could prove very promising for SQUID MRI: magnesium diboride, or MgB_2. This material has a relatively high transition temperature of 39 K and is notoriously easier to fabricate and engineer into wires and Josephson junctions than High-T_c cuprates [58] [59]. MgB_2 SQUIDs have been successfuly used in a clinical context as potential probes for magnetocardiography [60]. At the end of 2022 we started a PhD project in collaboration with the University of Turin on the topic of MgB_2 SQUID detection systems of NMR and MRI. The results of this research project could prove very valuable to design an even lighter MRI system, as the benchtop cryogenic machines required to cool the SQUID to about 30 K are a lot lighter, less expensive and less power-consuming than their 4 K counterparts. Recently, MgB_2 SQUID equivalent flux noise have been measured at 36.5 K, reaching 270 $\mu\Phi_0/\sqrt{\text{Hz}}$, which is very promising at such high temperatures [61].

4. **Other biomedical NMR devices.** NMR, and in particular low-field SQUID-detected NMR has enormous potential for diagnosis, patient monitoring, or screening in fields other, but related to MRI. Magnetic resonance relaxometry [62], for instance, is an old technique that is lot easier to implement than MRI at low fields and can prove extremely useful for screening. It is not so used in a traditional MRI scan where the MRI sequences are a lot more useful, but could prove all its potential when implemented in a portable, inexpensive device. Also, technologies measuring biomagnetism such as superparamagnetic relaxation, magnetoencephalography, magnetocardiography could very well benefit from a SQUID system with improved sensitivity, even if the operation outside a magnetically shielded room is still an open question. Finally, diagnosis techniques involving magnetic immunoassays, which use magnetic nanoparticles to label zones of interests (tumours for instance) could benefit from increases in signal-to-noise ratio from our detection technology, making them potentially viable at scale.

5. **Non-medical applications.** One big advantage of working at ultralow fields is the possibility to do an MRI in presence of metallic components. In traditional high-field MRI, gradients of high intensity of order 100 mT.m^{-1} are used, with switching times below 1 ms. If metallic parts are present, eddy currents are generated, which create a low of electromagnetic noise. On top of this, there is a great magnetic susceptibility difference between metallic and non-metallic parts of the sample. This causes magnetic field gradient artifacts that destroy the

linearity of the gradient field pattern used to perform MRI. All these problems are alleviated at low field where low gradient intensity of a few mT/m are used [42]. This makes a strong case for the use of ultra-low field MRI for patients with clips or pacemakers, and on the battlefield for soldiers with bullet wounds. Another very promising, non-medical application would be the imaging of a fully metallic sample. This is impossible with high-field MRI for the reasons stated above, but most importantly because of the skin effect of conductors. When a propagating electromagnetic field reaches a conductor/dielectric interface, eddy currents are created inside the conductor. These current in turn generate another magnetic field that compensate the incipient magnetic field. This make the total magnetic field effectively die out when going inside the bulk of the conducting sample. The *skin depth* δ is a measure of how deep the magnetic field can penetrate inside the metallic sample:

$$\delta = \sqrt{\frac{2\rho}{\mu_0 \mu_r \omega}}, \tag{25}$$

where ω is the pulsation, ρ is DC resistivity, μ_0 is the permeability of vacuum and μ_r is the relative permeability of the sample. Taking an order of magnitude of $\omega = 50$ MHz in traditional high-field MRI, the skin depth in most metals will usually lie below 100 μm, which makes MRI of metallic samples impossible. In the case of low-field MRI, however, working at frequencies that are 3 to 4 orders of magnitude lower means that we can get an increase of 30 to 100 on the skin depth to reach a few millimeters to a few cm, depending on the material's resistivity. This makes it possible to perform an image of a metallic sample, and could be used for inspection of electronic components, Li-ion battery health and charge monitoring [63][64], or metallic container inspection in sea transport.

Should we really use SQUIDs?

This question might look provocative given the scope of the paper, but designing and building an optimal SQUID readout chain takes a lot of time. Also, the limit under which low-T_c SQUIDs start to be better than inductive antennas is at a few 10 mT, not very far from the 1 mT field we plan to use. Therefore, it is a worthwile question to ask whether building a SQUID detection system is really worth the time and money investment at this stage. We believe the answer is yes, and below we give a few quantitative arguments to back it up.

Toy model

As a toy model we consider an inductive antenna of diameter $D = 10$ cm made of 1 mm commercial Cu wire, cooled down to 50 K. The number of turns in the coil is N, we start by considering the case $N = 1$. It has a DC resistance of $R = 1$ mOhm and an inductance of $L_a = 1$ μH. The SQUID we use is a STAR Cryoelectronics model SQ2600 with the following parameters: input coil inductance $L_i \simeq 2.5$ μH, equivalent input flux noise $n_{\Phi_0} = 3$ $\mu\Phi_0$ / $\sqrt{\text{Hz}}$, transfer coefficient $C_T = 200$ $\mu\text{V}/\Phi_0$, input coil coupling $1/M = 0.1$ $\mu\text{A}/\Phi_0$ and equivalent input current noise $n_i = 0.3$ pA / $\sqrt{\text{Hz}}$. The goal is to compare the performances of this antenna in two cases:

- Used as an inductive antenna coupled to a high impedance low noise voltage preamplifier,
- Used as a pickup coil for the SQUID magnetometer in a current-sensing configuration.

In these conditions, as we have $R << L_a\omega$, the impedance is dominated by the inductive part. The Johnson noise in the antenna is

$$\delta i_1 = \frac{\sqrt{4k_B T R}}{(L_a + L_i)\omega} \simeq 1.8\,\text{pA}/\sqrt{\text{Hz}}. \tag{26}$$

In any well-designed signal readout chain, each of the parts should contribute to a comparable degree to the total noise. Hence, as the equivalent input noise of the SQUID is $n_i = 0.3$ pA $/\sqrt{\text{Hz}}$, the noise in the pickup coil should be decreased by about one order of magnitude to take full advantage of the sensitivity of the SQUID. This can be achieved by using a pickup coil with a greater number of turns, as will be the case in our setup, where gradiometric coils are used. The equivalent tension noise in the coil is $\delta u_1 = \sqrt{4k_B T R} \simeq 2$ pV$/\sqrt{\text{Hz}}$. Most commercial preamps have input noises of order a few 100 pV $/\sqrt{\text{Hz}}$ at best[65], so it makes sense to consider using SQUIDs.

Now we should compare performances of the full systems in terms of detectivity threshold. The magnetic field in a $B_0 = 1$ mT NMR experiment is of order $B_2 = 100$ fT. The electromotive force induced in the antenna is $e = \omega B_2 S = 200$ pV, with $\omega = \gamma B_0$ and $S = \pi(D/2)^2$ the surface of the coil. In the case of inductive detection, this gives a signal $s_{\text{ind}} = \omega S = 2000$ V/T at the input of the preamp. Regarding the noise, the dominant contribution comes from the input noise of the preamp, $n_p \simeq 0.5$ nV $/\sqrt{\text{Hz}}$. In the case of inductive detection, we get a detection threshold

$$d_t^{(\text{ind})} = 250\,\text{fT}/\sqrt{\text{Hz}}. \tag{27}$$

In the case of the SQUID, the coil noise n_a dominates the SQUID's input noise. At the output of the SQUID,

the equivalent noise is

$$n_a^{(\mathrm{sq})} = MC_T \frac{\sqrt{4k_BTR}}{(L_a + L_i)\omega}. \tag{28}$$

Then, the output signal is given by

$$s_{\mathrm{sq}} = C_T S \frac{M}{L_a + L_i}, \tag{29}$$

which gives a detection threshold

$$d_t^{(\mathrm{sq})} = \frac{\sqrt{4k_BTR}}{S\omega} \simeq 3.5\,\mathrm{fT}/\sqrt{\mathrm{Hz}}. \tag{30}$$

With this toy model, the SQUID has a detection threshold about two orders of magnitude lower than inductive detection at 1 mT, which is big enough of an improvement to consider making the investment in hardware and development time for our device. Now let's see how this result changes with more complicated pickup coil geometries.

Adding more turns to the coil

The three parameters that are affected by the number of turns N in the coil is the coil's resistance R, which is proportional to N, the coil's inductance L_a, which goes as N^2, and the detection surface S, which is proportional to N. The detectivity threshold of a SQUID with N turns in the pickup coil is then simply proportional to $1/\sqrt{N}$. Naively, we would think then that we should increase the number of turns as much as possible to kill the Johnson noise, but this rule only holds up to the point where the Johnson noise becomes comparable to the intrinsic SQUID input noise n_i. In fact, this is a very general rule that in any well design detection chain, each part should contribute equivalently to the total noise.

The optimal number of turns in the pickup coil is found when comparing the two sources of noise:

$$n_a^{(\mathrm{sq})}(N_{\mathrm{opt}}) = n_i^{(\mathrm{sq})}(N_{\mathrm{opt}}), \tag{31}$$

which gives the implicit equation

$$N_{\mathrm{opt}} = \left(\frac{\sqrt{4k_BTRN_{\mathrm{opt}}}}{n_i L_a \omega} - \frac{L_i}{L_a} \right). \tag{32}$$

With our parameters, we find $N_{\mathrm{opt}} = 7.15$.

WHAT WE ARE DOING

In July 2021, two years ago, we set up our lab in the ESPCI, Paris, starting with nothing but an empty room. In just two years, we managed to build from scratch several iterations of a NMR-ready ultrasensitive SQUID antenna, the first version of an active noise cancellation system, and to run our first MRI sequences with inductive detection at 1 mT. While our first results can be explained in just a few paragraphs and figures, the physicists reading this will know that they are the product of a long series of trials, errors, and countless experimental problems to fix. We thought it would be a good idea to detail this journey for several reasons. First, for investors, future clients, and business partners to get a clear picture of what building an MRI machine with new-generation magnetometers involves. Secondly, to foster discussions with other physicists who might know solutions to our problems and would like to join the adventure!

We are lucky to have built a world-class team of young scientists and engineers covering a wide background of extremely hard topics. People in Chipiron have worked in the past on quantum phase transitions, integrable models, laser spectroscopy, bidimensional condensed matter, Deep Learning for protein folding, the Big Bang, and of course SQUIDs and MRI. This gives us the necessary creativity to constantly solve the problems that arises. To give us guidance on such complex topics, we secured some collaborations with seasoned scientists with whom we interact at least on a weekly basis:

- Fabrice Voisin from the laboratoire Astroparticule et Cosmologie (APC), of the Université Paris Cité. Fabrice is an expert of SQUIDs and low-noise electronics.

- Julien Kermorvant from Thales. Julien has expertise in SQUID detection systems, and has already performed MRI acquisitions with High-T_c multi-SQUID systems called SQIFs.

- Elodie Parzy and Eric Thiaudière from the Laboratoire Résonance Magnétique des Systèmes Biologiques of the Université de Bordeaux. Elodie and Eric worked for more than 20 years on low and ultra-low field acquisition strategies and MRI instrumentation.

- Stéphane Holé and Jérôme Lesueur from the ESPCI, who have expertise in SQUID fabrication and characterisation, as well as ultra-low field NMR involving SQUID detection. This very specific combination of technological bricks, as well as the very high standards of scientific excellence at the ESPCI is the perfect place for us to thrive.

Building a SQUID detector from scratch involves a lot of troubleshooting in electronics, cryogeny, mechanics, noise management, and countless other topics. Below we list a few of the main problems we had to deal with while building, and how we managed to solve them.

Work in the lab

Cryogeny

A SQUID being made out of superconducting material, it requires cooling to very low temperatures of 4 K to operate. There are two ways to go about this: you can use a cryogenic liquid as liquid Helium, which is getting more and more expensive ($2000 for a 100 litre container today versus less than $1000 three years ago) and is non-renewable. The other solution, which we chose, is to use a cryogenic machine, much like your kitchen's refrigerator. It consists of a compressor, which compresses gaseous Helium and sends it to a cryocooler, in our case a pulse-tube cryocooler, in which the gas expands and cools down a metallic plate on which you place the device you want to cool, in our case the SQUID chip. The Helium flow is in closed loop with no losses, which means there is zero Helium consumption. A pulse-tube cryocooler is preferred over other technologies such as Gifford-MacMahon or Stirling machines because they produce less mechanical vibrations, which would impact the noise levels. In our first experiment, we use a Sumitomo RP-082B2S with a F-70 compressor [66] which consumes about 8 kW of electrical power for a total weight of 150 kg, and provides 900 mW of cooling power at 4 Kelvin. This system has enough cooling power to allow us to try a lot of different antennas and SQUID configurations without worrying too much about constraints of performance of other parts of the system. This is a general trend with all the other parts of the experiment: to unlock the first technological bricks, we start with the most powerful instruments and hardware parts, even at the cost of a lack of transportability and high price. In the case of cryocooling, we estimate that we could easily cool the SQUID with 100 times less cooling power than what we have now. In the final product, a lighter cooling solution will be preferred to make the machine transportable and easy to use.

The SQUID is placed inside a sealed metallic box, the cryostat, from which you remove all the air with a vacuum pump to reach pressures of order 10^{-7} mBar, about ten billion times less that the ambient pressure. You need low pressure to ensure the SQUID doesn't heat up from convection and diffusion. Our first three cryostats have been built by MyCryoFirm, a cryogenic company close to our lab. On the second iteration, we added mechanical springs for microphonic noise reduction, while the third cryostat holds a RF-transparent composite part to accommodate a 40 K-cooled pickup coil to perform SQUID MRI on small field-of-view phantoms (80 mm). In parallel to these developments, we are working with the french company Absolut System in Grenoble to build a very-low consumption 4 K cryostat that will make the whole device truly portable. The first iteration of this portable cryostat will arrive in summer 2024.

Another topic is the cooling of the antenna itself with a big enough field-of view (200 mm or more). As we mentioned before, cooling the antenna helps to reduce the Johnson noise in conductors, allowing for an increase in SNR. We will perform this cooling with the first stage of our pulse-tube cryocooler, which produces 35 W of cooling power at 45 K. The idea is to implement a circulation of gaseous He, known for its very high cooling efficiency, which will cool down on the first stage of the pulse tube and circulate along the antenna in a specifically designed light and RF-transparent cryostat. We performed some thermodynamics and fluid mechanics simulations to dimension the system, in particular the radius of the pipes, cooling power required, and power of the mechanical pump. Reaching temperatures between 20 and 40 K, this will allow to reduce the Johnson noise sufficiently to go below the input noise level of the SQUID. These temperatures are also high enough to image room-temperature body parts with the antenna very close to the sample. This light cryostat project was just kickstarted in April 2023.

Dealing with SQUIDs

The reason we are using SQUIDs is, of course, because they have an exquisite sensitivity. This also means that installing and running a SQUID detection system requires a lot of precautions to properly thermalize the system and avoid picking up parasites.

All the leads to the SQUID, including the pickup coil, and the output cables have to be properly heat sunk. Contrarily to most SQUID experiments that are performed inside a wet cryostat using liquid He, we use a pulse-tube cryocooler and the SQUID is cooled on a cold metallic plate in vacuum. All the cables and SQUID have to be cooled with a thermal metallic link to the plate. This has to be done extremely carefully to avoid shorts, ground loops, and picking up parasites. This includes careful soldering, proper shielding of all cables, and the use of twisted pairs to reduce noise to the minimum. Because everything is metallic, it is very tricky to keep the pickup coil and the SQUID electrically floating and avoid to create ground loops while ensuring good thermalization. On top of this, it is useful to use cryogenic transformers for ground isolation of the SQUID [67]. Analog filtering in the input line is also important for two reasons: to improve the signal-to-noise ratio, and to prevent high-frequency signals from destabilizing the SQUID's feedback electronics. Typical noise picked up by the cables comes from instruments in the lab, elevators, passing cars or trains. In our case, the biggest source of noise was *microphony* from the pulse-tube cryocooler, which comes from induced current inside vibrating cables in an inhomogeneous background magnetic field. The cryocooler

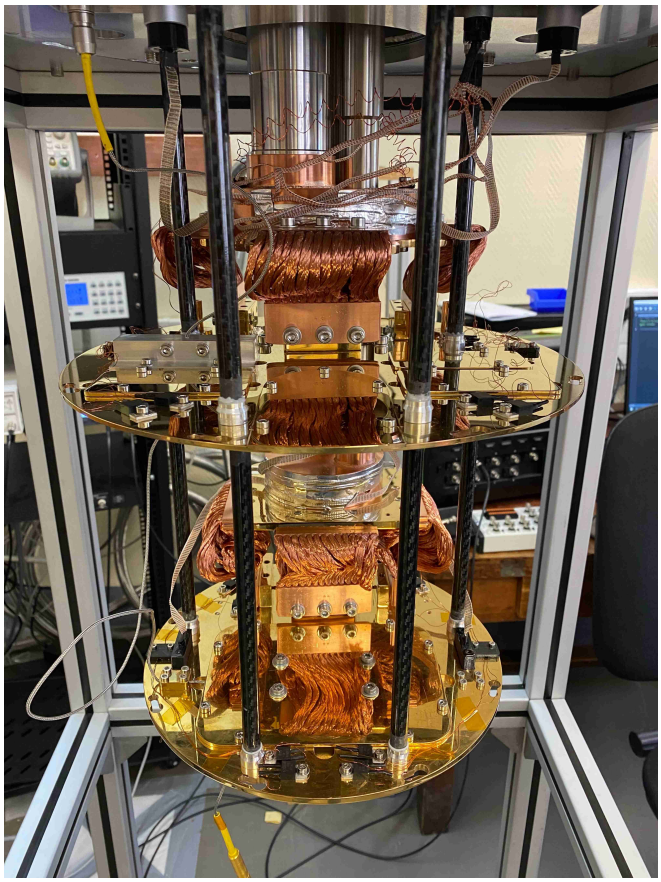

FIG. 15. The inside of our 4 K cryostat, where the SQUID and prototype cold antennas are cooled down. The top plate is at 40 K and will be used for the cooling of the antenna. The bottom plate is where the SQUID is cooled to 4 K. The copper braids and carbon pillars are used to limit the effect of vibrations that create microphonic noise.

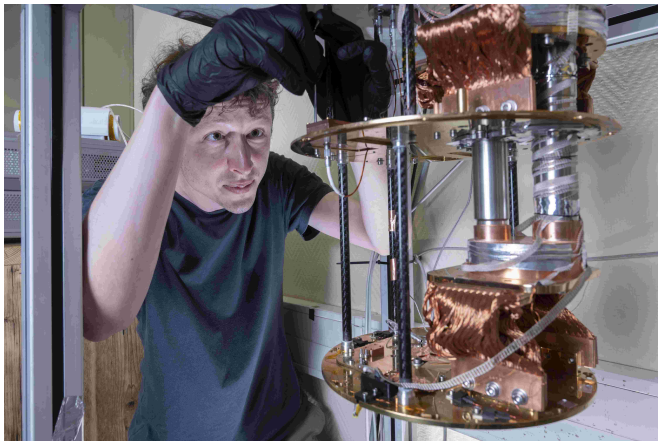

FIG. 16. Installation of a 50 K to 4 K input line connecting the pickup coil to the SQUID.

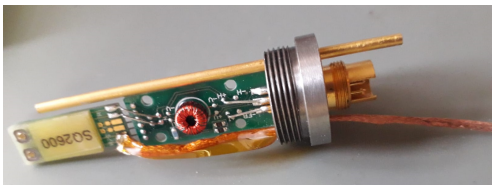

FIG. 17. A SQUID magnetometer, model SQ2600 of STAR Cryoelectronics mounted with readout electronics and a Niobium shield assembly (shield open on the picture). The SQUID chip is protected under the resin layer on the left side of the picture. The input coil can be accessed through the two Niobium pads, leads are introduced in the shield through the thin metallic tube on the top. We use a copper thread as a heat sink to properly thermalize the chip, by connecting it to the cold plate of the cryostat.

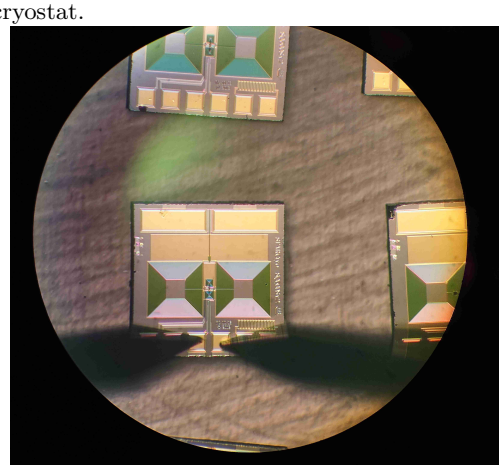

FIG. 18. Several washer design SQUID chips under the microscope. The two big squares on the chip are the input coil, the Josephson junctions of the SQUID can be seen between the two coils in the center. The different elements (feedback coil, SQUID output, input coil) are reached through the gold pads on the edges of the chip.

functions with a cycle of compression-decompression of Helium gas. In comparison with other similar cryocoolers like Gifford-MacMahon, pulse-tubes produce a lot less mechanical vibrations, because there are no moving metallic parts in the cold head. Still, there remains some unavoidable residual vibrations that propagate through the rigid parts of the cryostat,and the cables that are bound to it. There are three ways to curb microphonic noise:

- Using shielded cables, to limit the interaction with background magnetic fields.
- Using cables wound in twisted pairs. Locally, the currents created in each cable cancel each other, which limits the noise.
- Reducing mechanical vibrations to the minimum. For this last point, we modified our cryostat to tie the cold plates to the pulse-tube with copper

braids, as can be seen on fig. 15. This gives some flexibility to the structure and kills most of the very low frequency noise below 1 kHz.

Once the system is all set up with protected and well heat-sunk leads, we can start some magnetic detection measurements. First, you start by directly injecting some current in the input coil of the SQUID, either through the input coil via a low-noise stabilized current source, or via the feedback coil. This does not require a pickup coil to begin with. This first step is used to set the parameters of the readout electronics, mainly the gain of the pre-amplifier and flux lock loop. This allows to control the bandwidth of detection (which we want to keep up to 100 kHz in our case) and the dynamical range (less important because we measure very tiny signals of order 1 pT). One has to be very cautious with the amplitude of the current, anything above 100 μA can destroy the chip by creating a short between one of the input coils and the SQUID.

Now, the next step is to perform a magnetic detection experiment with a pickup coil, through radiative coupling. To start, it is easier to use a reduced-size pickup coil wound from superconducting Niobium wire, like in most SQUID MRI experiments. With this configuration, we can test the effect of the geometry in a very controlled environment, where the very low temperatures suppresses most of the Johnson noise. Also, we can enclose the detection system in a Pb box, Pb being superconducting below 7 K. Because of the Meissner effect, superconducting shields are extremely effective for magnetic shielding, much more than typical room-temperature magnetic materials. Then, once environmental and intrinsic noise has been reduced to a minimum, one can place a source of signal inside the shield, namely a small copper loop carrying a small alternating current at a given frequency. As SQUIDs are so sensitive, it is extremely important to reduce the noise to a minimum and to use very small signals for testing, as anything too intense will quickly put the flux-lock loop out of its operating range, and more generally saturate the detection system. With this configuration, we can safely compare the response of different sizes and geometries of flux concentrators with the same source and background noise, which gives as a result comparisons of signal-to-noise ratios. More details on this experiment in the next part.

To test our technology in a more realistic environment, we need to perform the same detection experiment with a full-scale Copper antenna at room temperature. In fact, in our final product, the antenna will have to enclose the sample of interest, in our case a part of the human body. With this configuration the antenna cannot be confined to the depths of the 4 K cryostat. Our simulations show that with a cylindrical antenna of typical length 30 cm and diameter 20 cm, it is realistic to cool the antenna down to 20 to 30 K while keeping the cryogenic requirements low enough to design a light, open design cryostat that can adapt to many parts of the body. This means that Niobium superconducting antennas are out of the questions, and that we will rather resort to high-quality Copper antennas, or, if our trials are successful, medium-temperature superconducting magnesium diboride (MgB_2) [68] antennas.

FIG. 19. Prototype of a copper volume gradiometer pickup coil.

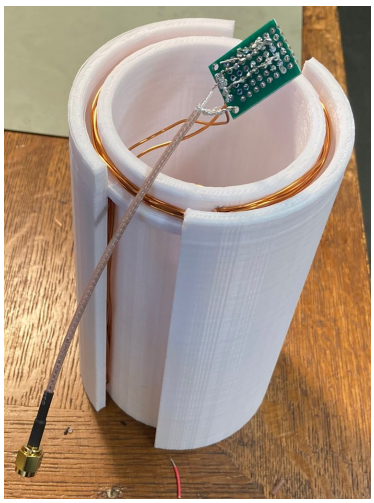

FIG. 20. Prototype of a Copper saddle pickup coil.

The first step is to build a room-temperature antenna, then progressively scale down the temperature first with liquid Nitrogen for simplicity, to reach 77 K, then with a light dry cryostat and a custom cryogenic system based on a pulse-tube cryocooler and gaseous Helium circulation to go below 30 K. We built some prototypes of Copper flux concentrators with 3D printed frames, that can be seen in fig. 19.

As was pointed out at the beginning of this part, running leads from the 4 K SQUID input to the room-temperature coil raises number of challenges: proper thermalization of cables, ground isolation, mechanical vibrations that turn into noise via microphony. We are

currently solving these problems with cryotransformers, careful wiring, and mechanical vibration reductions. To deal with the extreme sensitivity of the SQUID, in the cold 4 K case, we used superconducting lead shields to reduce environmental noise and allow us to use extremely weak signals. At room temperature, obviously, it is hopeless to use superconducting shields, hence active shielding strategies like the one described in [45] will be used.

Coil design

To increase the SNR of the SQUID MRI experiment, a key ingredient is the geometry of the flux concentrator. Going from a typical second-order gradiometer surface antenna to a volumetric geometry allows to gather more signal, while keeping a gradiometric configuration protects the detection system from outer noise.

There is a simple argument to be made regarding the potential SNR increase we can get with a volumetric geometry. Consider the toy model presented in fig. 21.

By the reciprocity principle, the sensitivity of an antenna to the field produced at a point M in space is proportional to the field created at M by the same antenna carrying a unit current. We will compare the antennas by considering the field produced at large distances z, representing faraway noise, and the field produced at close distances, representing the NMR signal. At large distances z on the axis, the (normalized) magnetic field produced by the surface or the volume antenna, $B_{\mathrm{s}}(z)$ and $B_{\mathrm{v}}(z)$ respectively, for unit current is:

$$B_{\mathrm{s}}(z) = 12 r_s^2 z^{-5} b^2, \tag{33}$$

$$B_{\mathrm{v}}(z) = 24 r_v^2 z^{-5} H_v b^2, \tag{34}$$

where quantities are defined in fig. 21. To compare the two antennas, we define $Q_{\mathrm{noise}} = B_{\mathrm{s}}(\infty)/B_{\mathrm{v}}(\infty)$, in our case

$$Q_{\mathrm{noise}} = \frac{r_s^2}{r_v^2}\frac{b}{2H_v}. \tag{35}$$

Then, the ability of the antenna to pickup a signal around the sample position is measured by its sensitivity around $z = 0$. We define $Q_{\mathrm{signal}} = B_{\mathrm{s}}(0)/B_{\mathrm{v}}(0)$, in our case

$$Q_{\mathrm{signal}} = \frac{r_v^2}{r_s^2}\frac{H_s^5}{2bH_v^4}. \tag{36}$$

The relative gain in SNR for our antenna can me measured by the function

$$\Gamma = \frac{\mathrm{SNR}_{\mathrm{vol}}}{\mathrm{SNR}_{\mathrm{surf}}} = Q_{\mathrm{signal}} Q_{\mathrm{noise}}, \tag{37}$$

putting everything together we get

$$\Gamma \sim \frac{1}{4}\left(\frac{H_s}{H_v}\right)^5 \sim 8. \tag{38}$$

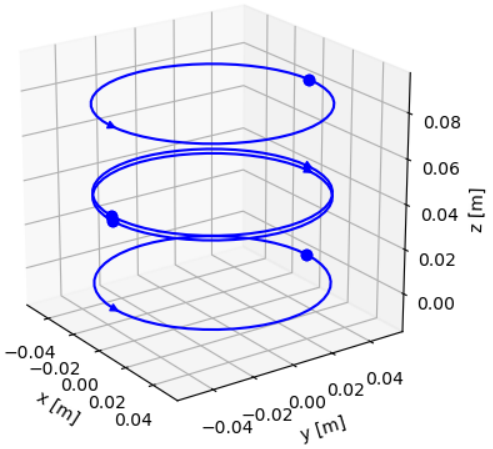

FIG. 21. Second order surface gradiometer with baseline $b = 4$ cm, radius $r_s = 5$ cm and distance from the base of the antenna to the sample $H_s = 20$ cm. These values are taken similar to common implementations of second order surface gradiometers in the literature.

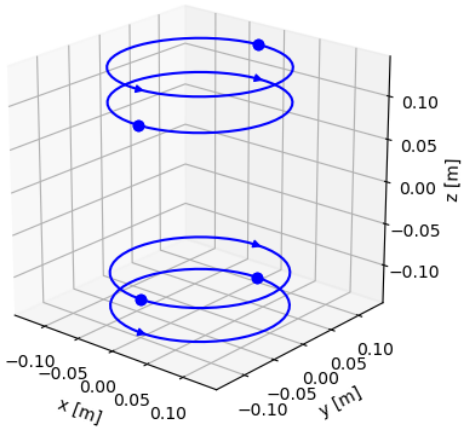

FIG. 22. Order one volume gradiometer with parameters baseline $b = 4$ cm, radius $r_v = 10$ cm and distance from the base of the antenna to the sample $H_v = 10$ cm. These values are close to the typical values we aim for for our first clinical application. Most importantly, the parameter H_v can be made a lot smaller in the volumetric case because the sample can be brought globally closer to the antenna.

This small calculation outputs a factor of 8 increase in SNR and shows that it is a good idea to try a volumetric geometry. This result stays qualitatively robust even if we consider noise coming from non-infinite distances, as is shown in fig. 23. The volumetric antenna acts as a order 1 gradiometer while the surface is an order 2, meaning we lose a bit of power in terms of noise rejection. How-

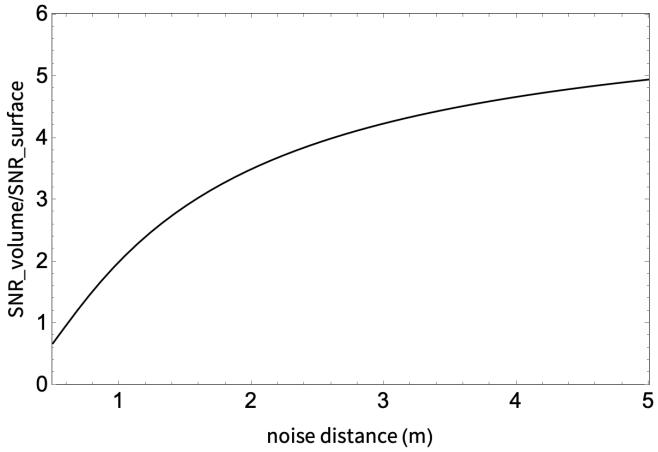

FIG. 23. Increase in SNR four our volumetric geometry compared to the usual surface case, as a function of the distance of noise sources. In a typical working environment (lab, hospital), most of the noise comes from instruments, power lines, or passing vehicles, that are at least a few meters away. An increase of at least 5 is a conservative figure to estimate what we would expect for a typical SNR increase.

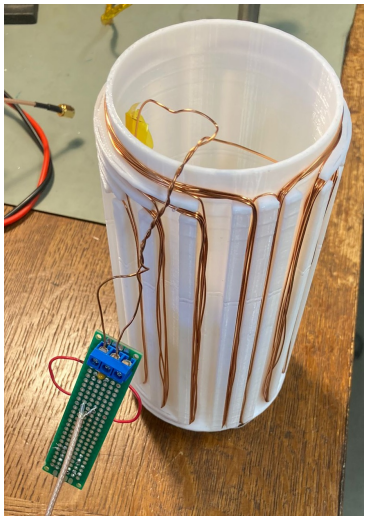

FIG. 24. Prototype of a copper RF transmit coil. This particular coil of the multi-saddle coil type is used for emission of the RF signal in the MRI experiment. We modelled this coil according to Nacher et al. [a]

[a] Nacher et al., The European Physical Journal D: Atomic, molecular, optical and plasma physics, EDP Sciences **310** 106638 (2019).

ever, the dominant factor is that in the volumetric case the antenna is globally closer to the sample, and this effect is leading the SNR increase. Of course, the precise details of the antenna, such as the type of geometry (saddle, birdcage, etc.), the material used, the cooling temperature, will be determinant and be assessed by further simulations and experimental data. Already, the first measurements we performed on cold Niobium antennas shielded in a 2-mm thick superconducting Pb shield (results to be presented at EUCAS 2023 in Bologna) shows this increase in SNR in good agreement with the previous formulas, but this remains to be confirmed by further data acquisition.

Another important parameter in the equation is the inductance of the pickup coil. It can be shown from simple electrokinetics that for a magnetic flux Φ_{ext} that is input on the pickup coil, the corresponding flux Φ_s seen by the SQUID is given by

$$\Phi_s = \frac{k\sqrt{L_s L_i}}{L_p + L_i}, \tag{39}$$

where (L_s, L_i, L_p) are the self inductances of the SQUID, the input coil, and the pickup coil, respectively. The SQUID and the pickup coil are coupled with a mutual inductance $M = k\sqrt{L_s L_i}$. The parameters L_s and L_i are fixed by the manufacturer of the SQUID chips, in our case for the model SQ2600 of STAR Cryoelectronics we have $L_i \simeq 2580$ nH and L_s is very small. Usually for a single-turn pickup coil with dimensions 10 cm or more, L_p will be in the range of a few μH to more than 10 μH, always above the value of L_i. In this case, as we want to maximize Φ_s for a given Φ_{ext}, it is always beneficial in terms of sensitivity to keep the inductance of the pickup coil as low as possible. This can be achieved in practice by using wires of greater diameter, and by keeping the size of the pickup coil as small as is allowed by the clinical application envisioned.

MRI coil design

Shifting a bit from magnetic detection, which is the core of our technology, let's talk a bit about how we design and choose MRI hardware. While there will be little innovation on this side compared to the SQUID detection system, we still have to design tailor-made coils and amplifiers that meet the specific requirements of low fields.

The first thing we can look at is the radiofrequency excitation system. We will be using very standard RF coils, from saddle to birdcage to more complex geometries to maximize homogeneity and efficiency, like the one described in fig. 24.

To power this coil, we need a RF amplifier that can provide high power pulses in a short amount of time to excite the spins of the sample via the RF coil. A cylindrical coil of diameter 20 cm and length 30 cm has volume of about 1 L, but coils for whole-body applications have bigger volumes, let's take a volume $V = 10$ L as a reference. This volume will be illuminated with a RF pulse of amplitude B_1 that tilts the spins of the protons in the transverse plane. With a RF pulse of duration τ, the flip angle α is simply $\alpha = \gamma B_1 \tau$. Let's take as a reference a field $B_1 = 10$ μT, which corresponds to a pulse dura-

tion $\tau = 600$ μs. The total electromagnetic energy E_0 required to generate this field B_1 over the volume V is

$$E_0 = V\frac{B_1^2}{2\mu}, \tag{40}$$

where μ is the sample's magnetic permeability, close to the permeability of vacuum μ_0. Generating this energy E_0 with a coil of inductance L and a current I requires an input energy

$$E_0 = \frac{1}{2}LI^2 \tag{41}$$

equalizing these two terms, with a coil of inductance 2.5 μH we need to provide a RF current of $I = 0.6$ A. In terms of power, with a $Z = 50$ Ohm output, we require

$$P = ZI^2 \simeq 16\,\mathrm{W}. \tag{42}$$

To be on the safe side, we chose to use a 150 W RF amp manufactured by the company RFPA in Bordeaux, France [69]. These amps are already light enough, in the future we will be able to lower the power rating to increase portability even further.

Now, regarding the gradient system, we choose to keep a very open geometry by using biplanar fingerprint gradient coils. The fingerprint design, presented in fig. 25, allows to drastically lower the inductance of the coils compared to a simple wire system, which lowers the voltage rating you need for the amplifier. Gradient amplifiers can very quickly become very heavy and power consuming if you don't plan in advance carefully your coil design. Again, to keep in mind the portability of the device, we chose to work with the model XPA-175-350 of IECO [70], which can provide a peak intensity of 175 A for a peak voltage of 350 V. The requirements of the system of gradient coils are the following:

- Linearity of the field below $+-5\%$ to keep image distortions to a minimum.
- Rise time of 250 μs for a maximum gradient amplitude of 5 mT/m, which gives a required slew rate of 20 T/m/s for the amplifier.
- Taking into account the duty cycle and pulse duration, we consider a maximum current of 70 A in the coils. Considering the slew rate and maximum gradient amplitude, this gives a limit of about 1 mH and 700 mOhm to the gradient coils.

Given these specifications, as well as the geometric constraints, we worked with our partners Pure Devices [71] to design custom biplanar gradient coils printed on PCB plates. PCB manufacturing is cheap and permits mass production of coils once when we start to scale the production. The results of the design are shown in fig. 25.

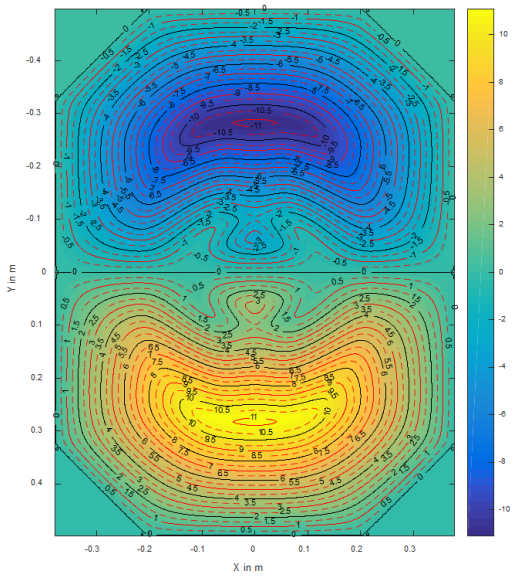

FIG. 25. Simulation results for the Y gradient plates with a fingerprint design. The dashed lines represent the mean path of the currents while the solid lines are the clearance lines between two current paths. The number on the lines represent local current density in arbitrary units. The gradient plates have simulated inductance $\simeq 0.2$ mH and DC resistance 130 mOhm, in accordance with the requirements. The peak Joule dissipated power is about 600 W, which should only require simple air cooling.

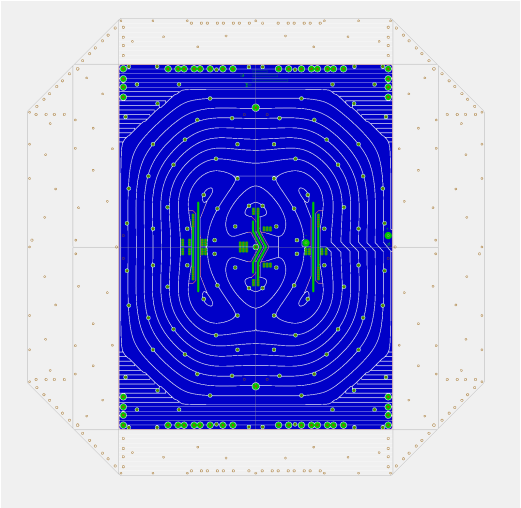

FIG. 26. A picture of the Z gradient PCB ordered from the manufacturer in accordance with the simulations.

Finally, we need a B_0 coil which is homogeneous enough while keeping low-consumption and portability features. To be on the safe side regarding homogeneity, we chose to start our first experiment with a copper square Merritt coil that delivers a 1 mT field (using a 40 A steady current) with 50 ppm homogeneity over a 20 cm wide field-of-view. The coils are 2 meters by 2 me-

FIG. 27. Discussions inside the B0 coil, the big PCBs serve as gradient plates. The RF transmit coil and pickup coils can be seen between the PCBs.

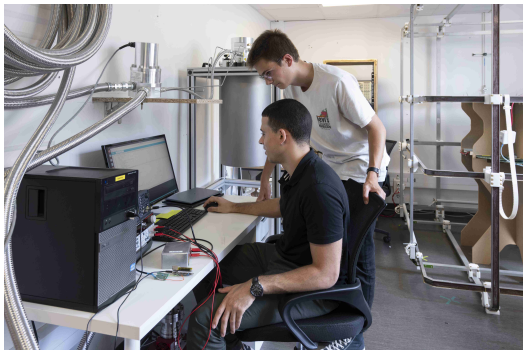

FIG. 28. The aluminium frames of the B0 coil from the outside.

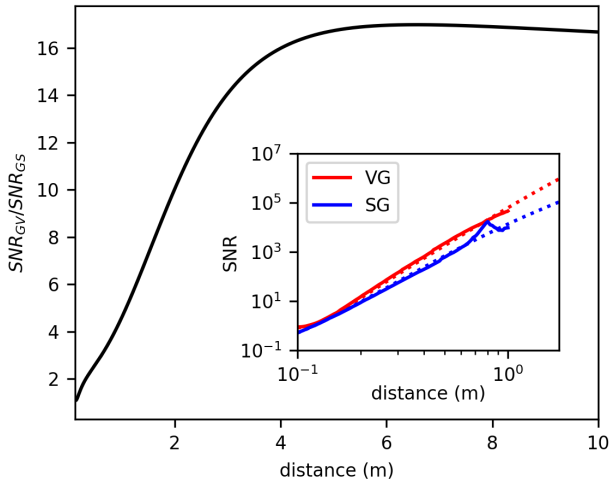

FIG. 29. **Main figure.** Numerical simulation of the ratio between the SNR obtained with the volume gradiometer and that of the surface gradiometer, with respect to distance. When the source is more than 4 meters away from the gradiometers, playing in that case the role of a noise source, the increase in SNR saturates to 16, which is the maximum SNR increase we can hope to get in an actual MRI experiment, where most noise sources are a few meters away from the field of view. **Insert.** Experimental data (full lines) and simulation (dotted lines) of the SNR increase between 10 cm and 1 m from the center of the volume gradiometer.

ters, and were designed and assembled in Spain by our partners at Serviciencia SLU. This set of coils is pretty far from transportable, but we want to start in the best conditions homogeneity-wise. This homogeneity figure can be degraded in the future with smaller coils, to increase portability, and using the gradient coils for order-1 shimming. At 1 mT, with 50 ppm homogeneity, we have

$$\frac{\gamma}{2\pi}\delta B_0 \simeq 2\ \text{Hz}, \tag{43}$$

which is smaller than $1/T_2$ for almost all tissues and hence does not degrade the T_2^* significantly. Regarding temporal stability, we use a feedback loop to keep the DC and very low frequency (below 100 Hz) within a 100 ppm range. This is detailed in the next section.

First results

Comparison between volume and surface pickup coils

To compare the SNR we can get with a volume pickup coil compared to a traditional surface one, we designed a simple experiment. The sinusoidal signal emitted by a small source is picked up by a SQUID detection system with a room-temperature gradiometric volume coil on one hand, and the same system with a surface gradiometer, on the other hand. We measure the SNR on the output voltage in both cases, and normalize the results by the coil's effective surface.

The experiment confirm the increase expected from simulations at short distances. The next iteration of the experiment will be close to reality with cooled down coils and a measurement range going to a few meters, which will be possible in our next facilities by the end of the year.

Sensitivity and stability of the detection chain

The current iteration of the SQUID detection chain is comprised of a room-temperature copper pickup coil, connected to the input coil of the SQUID via an input line going from 300 K to the 4 K plate inside the dry cryostat, comprising of a copper shielded twisted pair, a flux transformer, and a niobium shielded twisted pair leading to the input coil. The transformer is placed in a 1-mm thick Pb box for shielding, and has 25 μH on the primary, and 18 μH on the secondary, with no ferromagnetic core. This transformer is used to make the pickup coil electrically floating and cut the ground loops that destabilize the readout, the inductances being chosen to maximize the current transfer function. Tuning and matching ca-

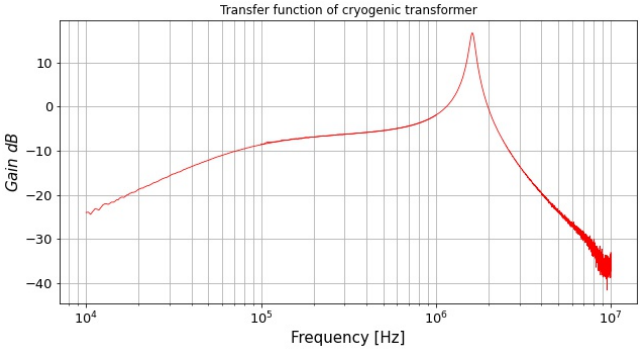

FIG. 30. Gain / frequency transfer function of the flux transformer. The gain at 42 kHz is -3 dB.

pacitors are also used for impedance matching.

We compared this version of the detection chain to a more conventional readout with a low-noise Femto voltage preamplifier. We get a SNR of the same order of magnitude, or slightly better with the SQUID readout. Our first results validate the possibility of using SQUIDs for MRI detection. We are currently working on the transformer efficiency and noise filtering in order to maximize the SNR.

The next iterations of the readout chain will consist of improving the gain of the transformer, cooling down the pickup coil down to about 50 K to reduce Johnson noise, and stabilize the readout to avoid jumps in the flux / tension characteristic of the SQUID with careful analog filtering.

First images

All of the acquisitions were performed using a room temperature pickup coil coupled to a 4 K SQUID detector (SQ2600, STAR Cryoelectronics), and a Pure Devices spectrometer for acquisition. The transmit coil is a saddle coil of inductance 21.0 μH and of quality factor $Q = 12.7$, while the receive coil is a gradiometric solenoid of inductance 25.0 μH and of quality factor $Q = 9.0$. The field is $B_0 = 1.0$ mT, stabilized with a PID loop on the measured magnetic field.

To obtain a first negative contrast image at 1 mT, a water-based phantom was built, consisting of a commercial paraffin candle (diameter 21 mm, length 130 mm) positioned coaxially inside a bottle (diameter 60 mm, length 130 mm) filled with doped deionised water (1.15 mM of MnCl2) as seen in Fig. 33. Both the phantom and the RF coils were positioned inside a 4-mm thick aluminium box, used for electromagnetic shielding. Then, we built a resolution phantom with more features, and produced first gradient echo images displayed in Fig. 35. In Fig. 37 you can see a first acquisition on a piece of lamb meat,

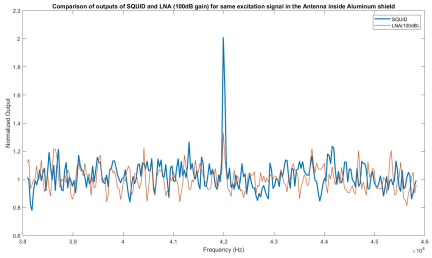

FIG. 31. Comparison of the voltage outputs of the two systems, the SQUID detection and the room-temperature voltage pre-amplifier, with respects to frequency, in normalized units. The preamp is set to 100 dB amplification. The two antennas are enclosed in an 7 mm thick Al Faraday shield and a sinusoidal signal at 42 kHz is sent out from a small emission coil. In this configuration, the SQUID amplification is on par, or better with a short margin, than the classical low noise voltage preamp counterpart.

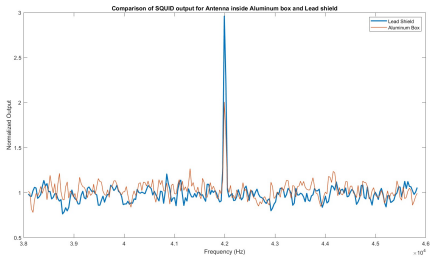

FIG. 32. Comparison between two type of shields, a fully closed Al box shield and a semi-open cylindrical Pb shield. The Pb shield displays a greater signal output, we believe for geometrical reasons, as it is a cylindrical shield whereas the Al shield has a parallelepipedic shape.

which will be improved to assess first anatomical details and implement fat-sat techniques.

Active noise cancellation

Definitions Because of low signal intensity and desired portability, our ultra low field MRI system suffers from high susceptibility to noise: this includes both internal noise, typically Johnson-Nyquist noise, and external noise, which is particularly present in unshielded environments. Reducing external electromagnetic noise can be done at several steps of a MR sequence, either analogically (compensating for the magnetic field noise using coils, subtracting the noise in the analog signal) or numerically during post-processing (denoising the MR signal using data driven methods and/or artificial intelligence). We summarize here current and future efforts to reduce EMI noise in post-processing. For this, we chose to apply methods for noise cancellation using external antennas [72] [45] [73] [74]. The general idea behind these

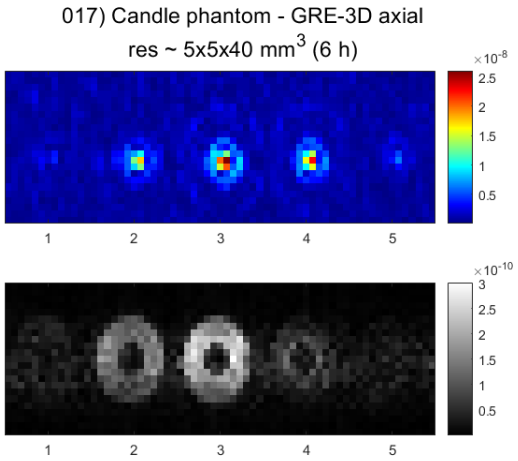

FIG. 33. Acquisition of a 3D GRE with our SQUID detection system. The sequence parameters are: T_R /T_E = 20/8.3 ms, flip angle = 70^o, matrix size = 23x13x5 pixels, spatial resolution ~ 5x5x40 mm^3, bandwidth = 217 Hz/pixel. With 16600 excitations, the whole acquisition lasted 6 hours. K-space filtering and in-plane interpolation into a 45x25 matrix were performed in post-processing.

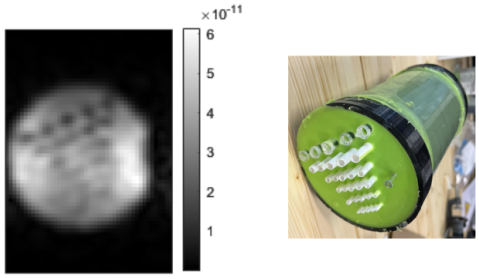

FIG. 34. 3D printed Resolution phantom, filled with water. There are air-filled tubes inserted of different diameters: 10, 8, 5, 4, and 3 mm respectively.

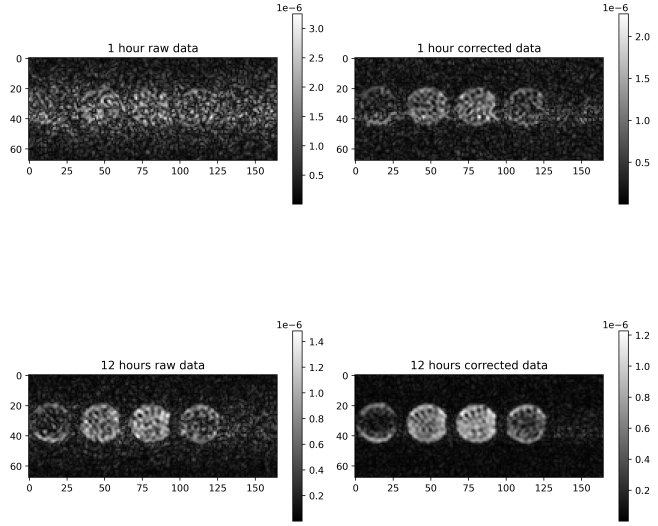

FIG. 35. Acquisition of a 3D GRE with our SQUID detection system. The sequence parameters are: T_R /T_E = 67/9 ms, flip angle = 90^o, matrix size = 101x17x9 pixels, spatial resolution ~ 10x10x30 mm^3, spectral width = 25 kHz. With 350 excitations, the whole acquisition lasted 1 hour (4200 averages for 12 hours).

FIG. 36. Lamb leg meat used for our first biological acquisition.

methods is to use external coils placed close around the MRI machine (and its R_x coil). These coils are made to sample the EMI noise present in the room during the MR sequence. The EMI noise is then digitally removed from the R_x coil signal. Of course, one needs first to establish a mapping between the noise signal as sampled by the external antennas on one hand, and the R_x antenna on the other.

Formally, we denote by S the signal coming from the receive R_x coil, and by $N_1, \ldots, N_c$ the noise signals acquired by the c surrounding coils. Following the original EDITER paper [72], it can be assumed that the signal S is a simple sum of the "pure" MR signal S^* and the EMI noise N:

$$S = S^* + N. \tag{44}$$

Here, other noise sources are excluded, or rather assumed part of the pure MR signal S^*. Of course, S^* and N are not known. In order to recover S^*, we want to compute a relationship $N = f(N_1, \ldots, N_c)$ so as to remove N from S.

Two types of methods exist for external coil based noise cancellation:

- The first category requires calibration data acquired outside the R_x acquisition, i.e. when $S^* = 0$. Indeed, this makes it easier to approximate the mapping f as an explicit function that can be applied to noise signals during imaging. However, this method requires a dead time to acquire the calibration data either before the MRI is started, or in between repetition times, thus increasing the minimum T_R achievable.

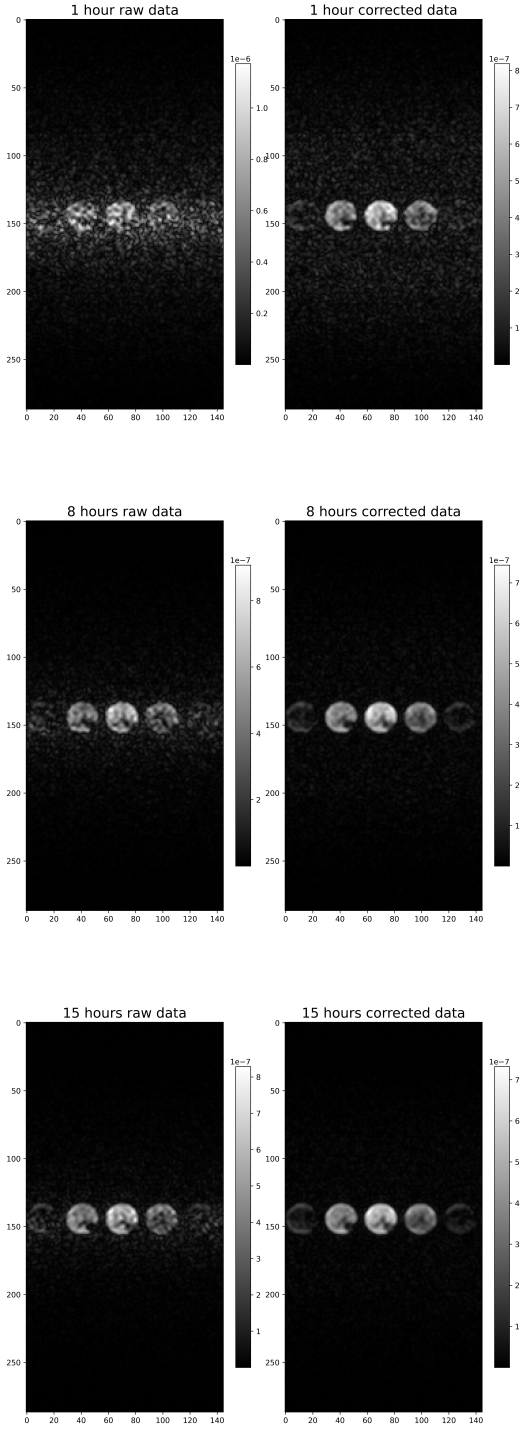

FIG. 37. Acquisition of a 3D GRE with our SQUID detection system. The sequence parameters are: T_R /T_E = 70/11.2 ms, flip angle = 70°, matrix size = 165x17x5 pixels, spatial resolution ∼ 10x10x60 mm^3. With 600 excitations (for 1 hour), the whole acquisition lasted 1 hour.

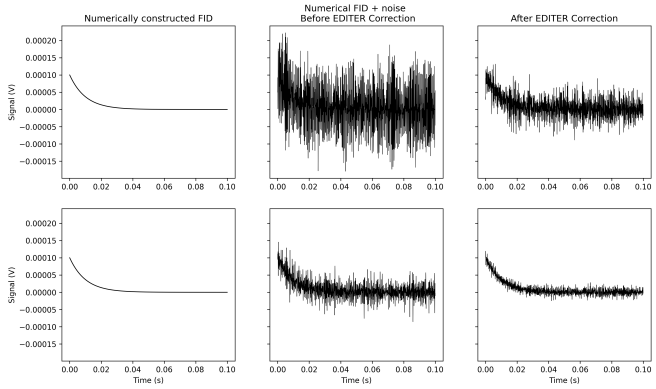

FIG. 38. EDITER denoising algorithm performance on mock signals after demodulation of noise signals. Numerical free induction decay (FID) with T_2 = 0.01 s and amplitude 0.1 mV. Up: Single shot FID. Bottom: Averaged over 10 shots.

- The second category does not require calibration data and is thus applied on the fly to the MR signal, making it in theory applicable to any MRI sequence. These methods often require the assumption of low correlation between S^* and N [72], or isotropy of the noise [74].

Preliminary results First, we assessed the efficiency of external coil based noise cancellation outside of the MRI setup.

A dataset of noise signals was generated using 7 coils: one central coil which plays the role of R_x, and $c = 6$ surrounding EMI coils. Two methods were tested:

- A linear convolution based method, EDITER, which is calibration free. EDITER was tested by artificially adding a numerical FID to the R_x coil signal.

- A deep nonlinear convolutional neural network (CNN) which requires calibration data for training. The network was thus trained on part of the generated dataset and tested on a separate part.

So far, both methods have achieved similar results in terms of amount of noise amplitude of the corrected signal, but EDITER's success seems more dependent on the initial SNR. More tests with poorly synchronized and/or differently post-processed signals (e.g. different tune and match setup, different demodulation and filtering etc) are ongoing.

One of the methods that can be used to numerically assess the performance of noise cancellation algorithms such as EDITER is to use the ratio of the remaining noise in the corrected signal over the original noise for a certain added numerical FID. More precisely, calling N the noise at the MR coil level, and having added an FID

S^* as the pure MR signal, this ratio is computed as:

$$R = \frac{\text{std}(S_{\text{EDITER}} - S^*)}{\text{std}(N)}. \quad (45)$$

Note that this ratio is computed in the absence of a real MR signal. On our mock signals, applying EDITER results in a ratio R of 30 to 40% (depending on the signal), meaning up to 60-70% noise reduction. CNN gave performances of R = 20-30%, thus beating EDITER, although being by definition a calibration based method, CNN's computed ratio is based on a null FID $S^* = 0$.

Integration of automatic noise cancellation into the MRI setup The current MR console we use for our experiments (Pure Devices) only has one analog input and can thus not be used to sample EMI signals from surrounding coils simultaneously as the signal from the R_x coil. We have thus opted to use an acquisition board for the EMI coil sampling, where synchronization between the two devices is achieved via a digital trigger.

The MRI console samples signals at the ADC frequency of 125 MHz, and internally applies demodulation with respect to the Larmor frequency, and a decimating filter to obtain filtered data at the requested sampling frequency (25 kHz). We apply similar operations to the data acquired via the acquisition board, so as to simplify the task of mapping signals from the EMI coils to the R_x coil. More precisely, the board samples signals at a frequency of $5*25 = 125$ kHz. We then apply demodulation and filtering before downsampling the data to 25 Ksamples/s. To avoid aliasing effects on the EMI data, a low pass analog filter with a cutoff frequency $f = 125/2 = 62.5$ kHz is included in the lines of the EMI coils.

So far two EMI coils have been placed around the R_x coil. Several positions and orientations of these coils have been tested to optimize noise cancellation. The current optimal positions are shown in Fig. 39. We have chosen to proceed with EDITER as it requires no calibration data and much less time for processing (computing the model and the corrected signals): 1 to 3 minutes for EDITER against 10 minutes for CNNs. The ANC protocol is thus fully integrated and can be used automatically with all sequences. Next paragraph shows results of this implemented setup on FID and 1D GRE sequences using the SQUID for amplification of the MRI signal.

Results We first tested our setup on FID sequences. Here we show results of an example FID sequence where EMI noise came from surrounding devices and sources. No EMI signals were added artificially. The sequence parameters were: $T_R = 60$ ms, $F_A = 90$. The data was composed of 1000 T_R shots, of 50 ms each, sampled at a 25 kHz frequency. Fig. 40 shows in frequency space the obtained signal from a single shot, 10 averaged shots, and 100 averaged shots.

Next, we tested our ANC setup on several 1D GRE runs which were also done using the SQUID in the MR

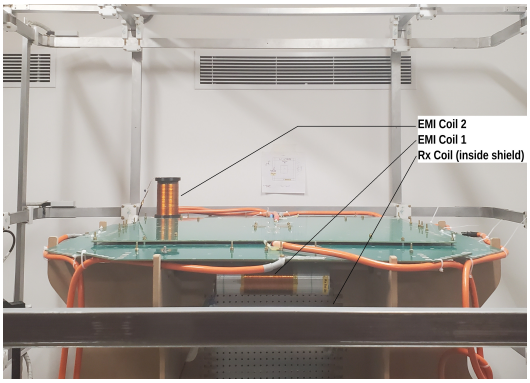

FIG. 39. Optimal position for the EMI coils.

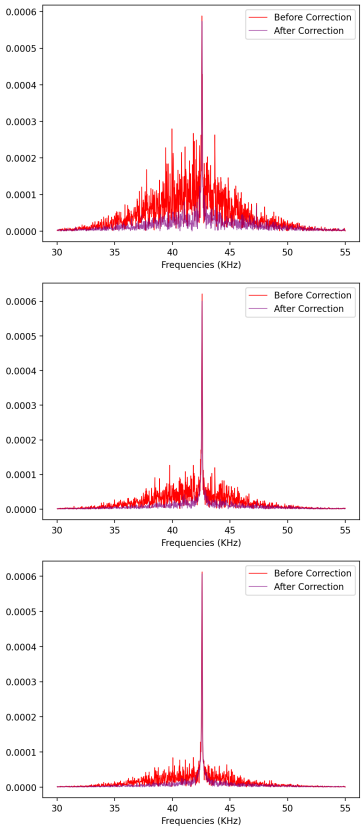

FIG. 40. Original (red) and EDITER corrected (purple) FID signals averaged over increasing number of shots. It can be observed that the EDITER corrected data shows fewer and smaller noise spikes. The correction ratio R for this run was R=0.7.

line. Currently, our usual 1D GRE runs have a resolution of 39 pixels over a 40 cm FOV, where the console data is acquired at 5 kHz with the corresponding readout duration to obtain 39 pixels. We observed that the ANC performance is suboptimal in these conditions, i.e. with few data samples per shot. To remedy this, we decide to double the readout duration and increase the console

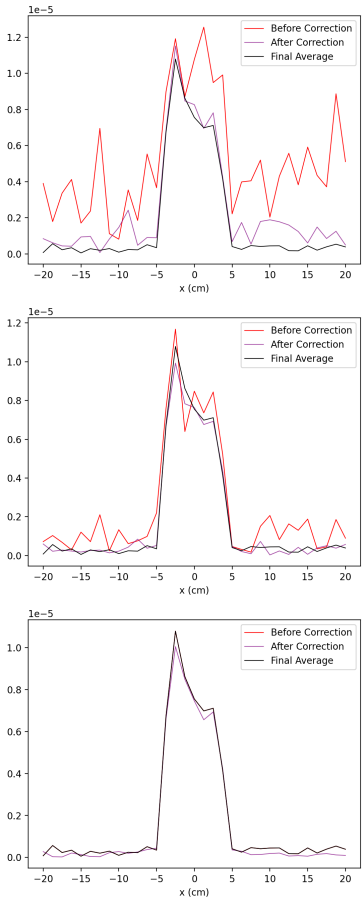

FIG. 41. Original (red) and EDITER corrected (purple) 1D GRE signals averaged over increasing number of shots. It can be observed that the EDITER corrected data shows fewer and smaller noise spikes.

sampling frequency to 25 kHz (the same as for FIDs) for the sake of noise corrections, thus having a 381 pixel 1D k-space. In theory, this would increase the FOV of the final image. However, we avoid this by going back to the downsampled k-space (i.e. to 5 ksamples/s) after correction and before taking the inverse Fourier transform. Results of ANC over one such 1D GRE run are displayed in Fig. 41. The sequence was 10 minutes long, use the gradient over the z dimension and 9000 shots were sampled. It can be seen that the corrected data, even after averaging very few shots, is well denoised and matched the final averaged data over 9000 shots.

Conclusions and future work The results currently obtained with ANC on FID and 1D GRE sequences are encouraging and show the importance of methods such as EDITER to reduce the electromagnetic noise in ULF MRI, thereby reducing the number of shots needed to obtain a good SNR. Future work includes increasing the number of EMI coils for more optimal sampling of all sources of noise, as well as testing the ANC setup over 2D and 3D sequences.

MRI reconstruction and trajectories

Sampling patterns There are three main competitors for the near future to accelerate acquisitions rather than using a conventional fully-sampled line-by-line Cartesian sampling:

- Line-by-line undersampling following a Gaussian distribution, typically over the 3rd k-space dimension (as done for example in [49]).
- Spiral trajectories, a non-Cartesian acquisition that can be easily parametrized to match sequence specifications (readout length, resolution, field of view, gradient constraints, etc). The k-space density can also easily be changed to reinforce specific regions.
- Segmented-EPI trajectories, as high field literature showed it can compete with much more complex non-Cartesian sampling patterns [75] such as SPARKLING. In low-field, acquisition windows will be reduced because of shorter T_1 and T_2, but it would still provide significant accelerations.

All mentioned trajectories can be combined with partial-Fourier acceleration, providing an extra multiplicative factor from 1 to 2 in an ideal case where the image phase is mostly static and composed of low image frequencies. Indeed, in the absence of perturbations the k-space is hermitian, and only half of it needs to be acquired. In a more realistic case we would sample most of the central-low frequencies, or would use scout images to account for low-frequency perturbations. In addition, planar non-Cartesian trajectories and EPI are compatible with GRAPPA acceleration, once we reach a setup compatible with parallel imaging using a large number of receiver coils. Our main focus for the moment is on EPI + Gaussian Undersampling.

Reconstruction Performances are currently assessed using simulations based on the M4Raw dataset [76] acquired at 0.3 T over 183 patients with 3 contrasts (T_1, T_2, FLAIR). The images are modified to account to various artifact sources, such as thermal noise matching the expected levels in our pipelines, observed B_0 inhomogeneities, etc.

Before reaching a setup compatible with parallel imaging and collecting datasets for deep learning, reconstruction algorithms are mostly limited to partial-Fourier reconstruction (typically with Projection Onto Convex Set / POCS [77] and all kinds of regularizations such as in Compressed Sensing (CS) (typically L1 norm over some wavelet domain). The same dataset is also being used to anticipate acquisitions with multiple repetitions, channels, but also for reconstruction using multiple contrasts [78].

Next steps Once target images on volunteers are available, we could easily use different machine learning approaches:

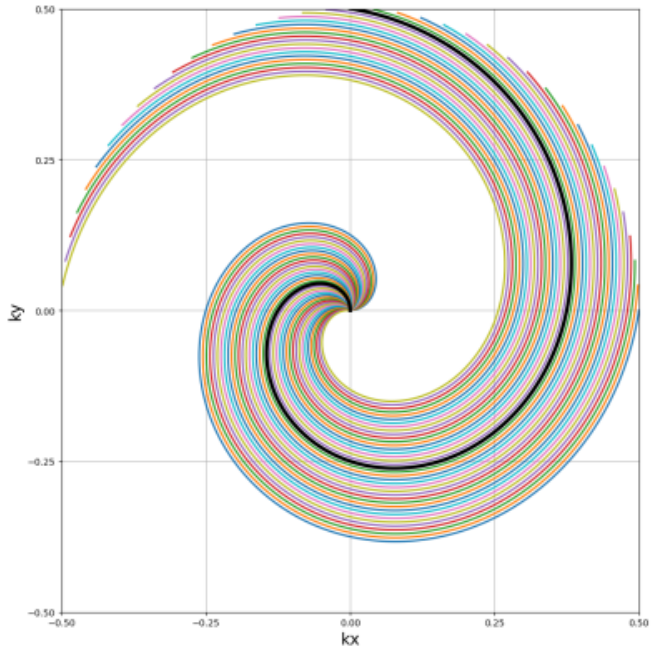

FIG. 42. This partial-Fourier spiral would be able to reach an acceleration factor of 4 over 4 ms readout windows with 10 mT/m gradients for an in-plane 2 mm target resolution, in the absence of concomitant gradients and under ideal circumstances (no phase disruption or purely static low-frequency phase disruption observed over scout images).

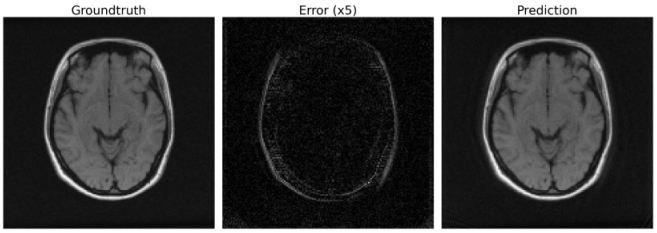

FIG. 43. Simulated results from the spiral acquisition of fig. 42. As a comparison, our competitor Hyperfine reaches an acceleration factor of 3.5 using Deep Learning based strategies [a].

[a] J. Schlemper *et al.*, ISMRM proceedings 0991 (2020).

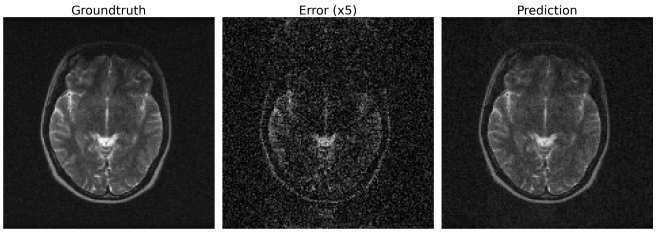

FIG. 44. Simulation of a 2D EPI 2x2mm^2 acquisition of a T_2-weighted contrast with an acceleration factor of 3, an acquisition window of 9 ms, and a gradient strength of only 4 mT/m. The simulation is carried out using the shorter T_2^* expected at low field.

- Variational networks, such as the approach used by Hyperfine in this recent abstract 43. It is the classic MR-specific approach with neural networks, and most state-of-the-art approaches are more or less subtle variations of that same structure [79].

- Data-driven trajectory learning, and even jointly learned trajectory and reconstruction networks. Some examples are BJORK, PILOT or PROPELLER, with a preference for BJORK [80] as it accounts for gradient constraints as a regularization, meaning that gradient strengths and slew rates are minimized beyond just the hardware constraints, as opposed to projection used in PROPELLER. This specific point helps a lot with concomitant gradients, as they tend to be more significant when using larger and more chaotic gradients for acquisition.

- Diffusion and score-based learning [81] to provide trajectory-independent deep learning reconstruction methods.

Simulated clinical images

To be able to anticipate the SNR needed to produce useful images, down below we provide realistic estimations of what organic images would look like for different target SNRs based on data/measure-driven simulations.

The simulation is based on the $630 * 630$ knee image showed in Fig. , with a roughly estimated resolution of around 0.3 mm^2.

FIG. 45. Reference knee image for our simulation.

The image is then processed as follows:

- Crop the top and bottom black bands.

- Lower the resolution to the target resolution given as input by reducing the k-space area.

- Apply a decay over the k-space lines that corresponds to a normalized decay obtained from real FID acquisitions. This step is not impacting much the simulation as the chosen readout window is quite short and placed early over the signal lifespan (start time: 3 ms, readout window: 2 ms).
- Add Gaussian noise after several steps of normalization:
    1. Multiply to match the noise levels observed in the previous FID (noise is defined as whatever is measured after 1500 ms).
    2. Multiply (and divide) by the number of target repetitions (and measured repetitions during the FID). The target number of repetitions is based on the allocated time of acquisition, T_R, number of slices and resolution.
    3. Multiply (and divide) by the estimated number of protons in the target knee slice (and in the measured "candle" sample shown in Fig. 33).
    4. Multiply (and divide) by the peak k-space value in the original image (and the measured FID at $t = 0$).
    5. Divide by an arbitrary SNR boost factor given as input.
- Apply zero-padding in k-space to artificially increase the resolution.
- Apply Gaussian convolution to smooth zero-padding artifacts.

The acquisitions were simulated for 4 setups corresponding to expected results over the course of the next few semesters, showed in Fig. 46.

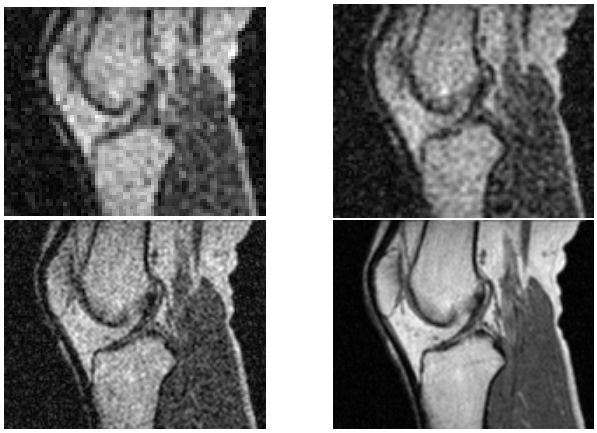

FIG. 46. Top to bottom, left to right: simulations of knee images obtained with our setup in the next few semesters, showing expected improvements every 6 months. The expected acquisition times, cumulated SNR gains and corresponding resolutions are (24h, 1, $4*4*8$ mm^3), (6h, 4.5, $3*3*6$ mm^3), (1h, 58.5, $2*2*4$ mm^3) and (10min, 643.5, $2*2*4$ mm^3), respectively.

FIG. 47. Eva and Isabelle discussing the results of a CPMG MRI sequence.

CONCLUSION

We believe the only way to improve MRI accessibility radically is to go for very low magnetic fields. However, for the past forty years, low-cost imaging projects have been crippled by the unsatisfying quality and duration of imaging sequences. Unfortunately, today low-field MRI is too often associated with low-quality in the mind of the medical imaging community.

We are changing this paradigm. Low field MRI has some invaluable advantages over high-field, that go way beyond just a drastic reduction in cost. The open, transportable nature of the device allows a whole new range of applications in emergency neuroimaging, mass screening for cancers or endometriosis, per-operatory imaging, or even imaging at the bedside or in a moving ambulance truck. It unlocks the access to quality medical imaging for people suffering of claustrophobia, obesity, or carrying metallic implants. Also, it gives access to MRI in zones that are impossible to reach by traditional high-field machines: remote places, countries where electricity supply is unstable, the battlefield... which accounts for 90% of the world's population. Finally, and perhaps most importantly, the ultra-low field range, below 1 mT, opens up a whole new realm or applications that are only physically possible at this field. At 1 mT and below, it is possible to use a resistive magnet and to tune the polarization field for fast field cycling, which is not possible with the permanent magnets of the intermediate fields of ~ 50 mT. Also, T_1 contrasts are notably enhanced, and it is possible to make images in presence of metal or even of fully metallic samples.

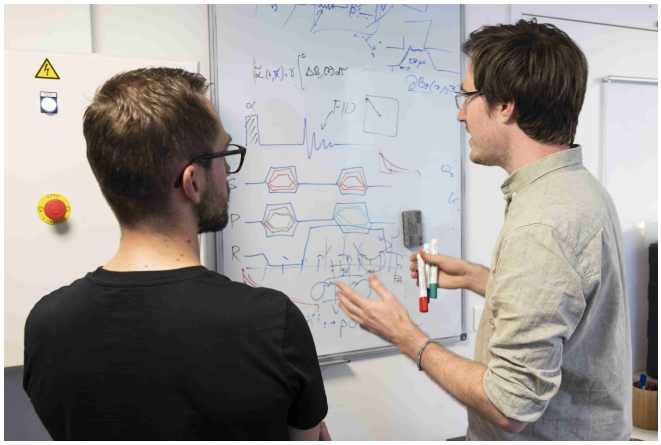

FIG. 48. Marco and Romain theorizing on low-field contrasts.

FIG. 50. Zineb at the workshop.

FIG. 49. Ijee and Yacine debating on the results of a SQUID magnetometry experiment.

FIG. 51. The Chipiron team.

By building the world's first viable ultra-low field MRI with true diagnosis power, our mission is to make MRI as common and simple as blood sampling, allowing prevention and medical imaging availability at scale. The combination of innovative volumetric antennas, low-T_c SQUID, active magnetic shielding, and the development of rapid low-field sequences and post-processing are our structural solution to make it a reality. This technology will also be applied to problems in the defence and automotive that can be some interesting markets in the future, but the core of our focus is to develop a versatile machine that will be used in clinical imaging.

Finally, and most importantly, our devices will be of great synergy with high-field machines: the information one gets from a high-field or a low-field scan are fundamentally different. We imagine our light and portable machines to act as a first intention device to use. One will never get the same spatial resolution in a 1 mT or a 7 T MRI scan, and for some precise details, particularly in neuroimaging, you need extremely fine resolution. Hence, high-fields will probably always be around, at least for research topics and other specific use cases. On the other hand, the superiority of contrasts (notably T_1 contrasts) at very-low fields will be, we believe, a game changer in developing new sequences for most routine use cases of MRI, making Chipiron MRI machines a powerful asset for radiologists globally.

* Corresponding author: dimitri@chipiron.co

[1] Only one proton in a million gets polarized at $B_0 = 1$ T, this figure drops to one in a billion at 1 mT.

[2] For more details see part on classical or quantum antennas.

[3] Strong difference in magnetic susceptibilities create local magnetic field gradients that destroy the field homogeneity and the linearity of the imaging gradients.

[4] Some research-oriented products are set to work at 7 T (only 90 units worldwide) while the NeuroSpin experi-

FIG. 52. Evan and Dimitri, the founders of Chipiron.

ment in Saclay, south of Paris, aims at a groundbreaking 11, 7 T for research in neuroscience.

[5] We neglected auto-inductance phenomena for simplicity of discussion.

[6] See eg. the datasheet of sensors from the website of STAR Cryoelectronics.

[7] W. Myers et al., J. Mag. Res **186**, 182-192 (2007).

[8] D. Drung et al., dc SQUID readout electronics with up to 100 MHz closed-loop bandwidth, in IEEE Transactions on Applied Superconductivity, vol. 15, no. 2, pp. 777-780, June 2005.

[9] Dang et al., Appl. Phys. Lett. **97**, 151110 (2010).

[10] Savukov et al., Appl. Phys. Lett. **103**, 043703 (2013).

[11] Herreros et al., Review of Scientific Instruments **84**, 095116 (2013).

[12] A. Doll et al. Proceedings Volume **11090**, Spintronics XII; 110903M (2019).

[13] Thesis of Samson Lecurieux-Lafayette, `https://www.theses.fr/2021UPASP147`.

[14] P. Hemmer et al., Science **339**, Issue 6119 pp. 529-530 (2013).

[15] Around -270 ^{o}C.

[16] Or its alloys, most commonly NbTi or Nb_3Sn.

[17] This is what happens in a laser, for instance.

[18] To make things not too technical, we will stick to a semi-classical discussion. Of course, like we just said, electrons are not free in a superconductor, but this simple model gives the right phenomenology for the current / tension relation.

[19] Recall that the electrical intensity is the flux of the current density through the section S of the conductor.

[20] It is interesting to note that the current density is a well-defined quantity while the vector potential is only defined up to a vector field of null gradient... The equation only remains true in the Coulomb gauge, and is hence non-gauge invariant. It remains approximately true in the case of a smoothly spatially varying magnetic field.

[21] A symmetry in physics is a group of transformations that leaves the system invariant.

[22] Without going too much into details, the phase $\phi(r)$ represents the gap of the wavefunction, which is a quantity that we measure in experiments in superconductivity.

[23] We are interested in DC SQUIDs, RF SQUIDs will not be discussed here.

[24] `https://www.theses.fr/175465479`.

[25] J. Clarke and A.I. Braginski, The SQUID handbook vol. 1, Wiley-VCH.

[26] Fagaly et al., Review of Scientific Instruments **77**, 101101 (2006).

[27] Gruber et al., J Magn Reson Imaging. **48**(3): 590–604 (2018).

[28] Vadim S. Zotev et al., Supercond. Sci. Technol. **20** S367 (2007).

[29] Penanen et al., Review of Scientific Instruments **85**, 094302 (2014).

[30] Hsin-Hsien Chen et al. J. of Applied Physics **110** 093903 (2011).

[31] R. McDermott *et al.*, J. of Low Tem. Phys. **135**, 793-821 (2004).

[32] V. S. Zotev *et al.*, J. Mag. Res. **194**-1, 115-120 (2008).

[33] Espy et al., IEEE Transactions on applied superconductivity **25**-3 (2015).

[34] `https://www.aalto.fi/en/department-of-neuroscience-and-biomedical-engineering/meg-mri-brain-imaging-group`.

[35] Sarracanie et al., Front. Phys. **8**, 172 (2020).

[36] B. Inglis et al., PNAS **110**-48, 19194-19201 (2013).

[37] D. Oyama et al., J. Mag. Soc. of Japan **47**-4 118-127 (2023).

[38] N. Bloembergen, E. M. Purcell, and R. V. Pound, Physical Review **73**, 679 (1947).

[39] S.K. Lee et al., Mag. Res. Med. **53**, 9-14 (2005).

[40] Körber et al., Supercond. Sci. Technol. **29** 113001 (2016).

[41] `https://sustera.securesite.jp/DL35-e.html`.

[42] S. Ouanani et al., J. Phys.: Conf. Ser. **507** 042008 (2014).

[43] Sarracanie et al., Scientific Reports **5** 15177 (2015).

[44] S. Busch et al., Magnetic Resonance in Medicine **67**-4, 1138-1145 (2012).

[45] A. Tong et al., Abdominal Radiology **45**, 1569-1586 (2020).

[46] Yilong Liu et al., Nature Communications **12** 7238 (2021).

[47] Qingqian Guo *et al.*, Concepts Mag. Res. Part B, Mag. Res. Eng. **882329**, 11 pages (2020).

[48] C. Lazarus et al., SPARKLING: variable-density k-space filling curves for accelerated-weighted MRI. Magn Reson Med. **81**: 3643-3661 (2019).

[49] This technique maps measured NMR signals to simulations. See Dan Ma *et al.*, Nature **495** 187-192 (2013).

[50] Sarracanie et al., Investigative Radiology **57** (4), 263-271 (2021).

[51] Sushentsev *et al.*, PLoS ONE **16**(1), e0245970 (2021).

[52] Trotier AJ, Rapacchi S, Faller TL, Miraux S, Ribot EJ. Magn Reson Med. 2019 Jan;81(1):551-559. doi: 10.1002/mrm.27438. Epub 2018 Sep 9. PMID: 30198115.

[53] Trotier AJ, Lefrançois W, Ribot EJ, Thiaudiere E, Franconi JM, Miraux S. Magn Reson Med. 2015 Mar;73(3):984-94. doi: 10.1002/mrm.25201. Epub 2014 Mar 10.

[54] Dallaudière B, Ribot EJ, Trotier AJ, Loubrie S, Dallet L, Thibaudeau O, Miraux S, Hauger O. Eur Spine J. 2021 Feb 20. doi: 10.1007/s00586-021-06755-x. Online ahead of print.

[55] Castets CR, Lefrançois W, Wecker D, Ribot EJ, Trotier AJ, Thiaudière E, Franconi JM, Miraux S. Magn Reson Med. 2017 May;77(5):1831-1840. doi: 10.1002/mrm.26263. Epub 2016 May 12.

[56] D. Prele *et al.*, IEEE transactions on applied superconductivity **19**, no. 3 (2009).
[57] Couedo *et al.*, Appl. Phys. Lett. **114**, 192602 (2019).
[58] Sung-Hak Hong et al., Physica C: Superconductivity and its applications **470**-1, S1036-S1037 (2010).
[59] A. Brinkman et al., Physica C: Superconductivity **456**-1-2 188-195 (2007).
[60] Superconductors: Properties, technology, and applications, Y. Grigorashvili, InTech, 2021, chapter 18: MgB_2 SQUID for magnetocardiography.
[61] L. Lolli et al., Supercond Sci. Technol. **29** 104008 (2016).
[62] R. Damadian *et al.*, tumour detection by nuclear magnetic resonance, Science **171** 3976:1151-3 (1971).
[63] K. Romanenko *et al.*, PNAS **116** (38) 18783-18789 (2019).
[64] A. J. Illott *et al.*, Nat. Comm. **9** 1776 (2018).
[65] In our setup we use the Femto model DLVPA, 100 kHz bandwidth and input noise 0.4 pV $/\sqrt{\text{Hz}}$.
[66] `https://www.shicryogenics.com/product/rp-082b2s-4k-pulse-tube-cryocooler-series/`.
[67] For instance the devices of CMR-direct `http://www.cmr-direct.com/en/cryogenic-transformers/ltt-m`. It is also possible to wire them directly in the lab, though a lot of care has to be given to the choice of a magnetic material that can sustain cryogenic temperatures, as well as proper shielding with Pb or Nb.
[68] A PhD project on this topic will be co-hosted by Chipiron starting end of 2022.
[69] `https://www.rfpa.com/`.
[70] `https://www.ieco.fi/index.php?k=10909`.
[71] `https://www.pure-devices.com/`.
[72] Srinivas *et al.*, Mag. Res. in Med. **87**-2, 614-628 (2022).
[73] Su *et al.*, IEEE Transactions on Medical Imaging **41** (5), 1007-1016 (2022).
[74] Parsa *et al.*, J. Mag. Res. **346** 107355 (2023).
[75] P. Sati *et al.*, Multiple Sclerosis J. **20** (11) 1464-1470 (2014).
[76] M. Lyu *et al.*, Scientific Data **10**, 264 (2023).
[77] G. McGibney *et al.*, Mag. Res. Med. **30** (1) 51-59 (1993).
[78] J. Huang *et al.*, Mag. Res. Im. **32** (10), 1344-1352 (2014).
[79] Z. Ramzi *et al.*, Applied Science **10** (5) 1816 (2020).
[80] G. Wang *et al.*, IEEE Transactions on Medical Imaging **41** (9) 2318-2330 (2022).
[81] M. Zach *et al.*, arXiv:2210.13834v3 (2023).